

# Developmental Cajal-Retzius cell death contributes to the maturation of layer 1 cortical inhibition and somatosensory processing

Received: 26 July 2023

Accepted: 11 July 2024

Published online: 01 August 2024



Angeliki Damilou<sup>1,2,3</sup>, Linbi Cai<sup>1,3</sup>, Ali Özgür Argunşah<sup>1,3</sup>, Shuting Han<sup>3,4</sup>, George Kanatouris<sup>1,3</sup>, Maria Karatsoli<sup>1,2,3</sup>, Olivia Hanley<sup>1,3</sup>, Lorenzo Gesuita<sup>1,3</sup>, Sepp Kollmorgen<sup>2</sup>, Fritjof Helmchen<sup>1,2,3,4</sup> & Theofanis Karayannis<sup>1,2,3</sup> ✉

The role of developmental cell death in the formation of brain circuits is not well understood. Cajal-Retzius cells constitute a major transient neuronal population in the mammalian neocortex, which largely disappears at the time of postnatal somatosensory maturation. In this study, we used mouse genetics, anatomical, functional, and behavioral approaches to explore the impact of the early postnatal death of Cajal-Retzius cells in the maturation of the cortical circuit. We find that before their death, Cajal-Retzius cells mainly receive inputs from layer 1 neurons, which can only develop their mature connectivity onto layer 2/3 pyramidal cells after Cajal-Retzius cells disappear. This developmental connectivity progression from layer 1 GABAergic to layer 2/3 pyramidal cells regulates sensory-driven inhibition within, and more so, across cortical columns. Here we show that Cajal-Retzius cell death prevention leads to layer 2/3 hyper-excitability, delayed learning and reduced performance in a multi-whisker-dependent texture discrimination task.

Like a building that relies on temporary structures as it is assembled, the brain sets up early transient circuits that can support its development. These transient circuits are mediated either by connections between cells, which are lost during development or by elimination of cells through cell death, commonly known as programmed cell death (PCD). Cell death is a crucial step for a plethora of developmental processes across species, as it drives morphogenesis and tissue sculpting; notable examples are the formation of the neural tube and the removal of inter-digital webbing respectively<sup>1,2</sup>. In the mammalian brain, a large proportion of neurons die during development<sup>3–5</sup>; most neuronal types experience loss of a fraction of cells, while some types

exist transiently and entirely disappear<sup>6–8</sup>. The role of such transient populations in the structural and functional development of cortical circuits is not well understood.

Cajal-Retzius cells (CRs/CR) represent a major transient cell population in the neocortex of many species, including humans<sup>9,10</sup>. They are produced during embryogenesis in multiple germline regions (septum, hem, ventral pallium, thalamic eminences) and are among the first cells to arrive in the developing marginal zone (future layer (L) 1) of the neocortex and hippocampus<sup>11–13</sup>. Embryonically, CRs have been found to assist in the inside-out formation of the cortical layers through reelin secretion, which regulates the migration of

<sup>1</sup>Laboratory of Neural Circuit Assembly, Brain Research Institute (HiFo), University of Zurich, Winterthurerstrasse 190, CH-8057 Zurich, Switzerland. <sup>2</sup>Adaptive Brain Circuits in Development and Learning (AdaBD), University Research Priority Program (URPP), University of Zurich, Zurich 8057, Switzerland. <sup>3</sup>Neuroscience Center Zurich, Winterthurerstrasse 190, CH-8057 Zurich, Switzerland. <sup>4</sup>Laboratory of Neural Circuit Dynamics, Brain Research Institute, University of Zurich, Winterthurerstrasse 190, CH-8057 Zurich, Switzerland. ✉e-mail: [karayannis@hifo.uzh.ch](mailto:karayannis@hifo.uzh.ch)

glutamatergic and GABAergic neurons, as well as oligodendrocyte cells<sup>14–19</sup>. CRs are nevertheless not mere reelin-secreting cells, but are embedded into the cortical circuit before their death, receiving anatomical inputs from glutamatergic and GABAergic neurons<sup>20–23</sup>, in turn innervating layer (L) 2/3 and 5 pyramidal cells and, to a lesser extent, other layer 1 neurons<sup>24,25</sup>. Focusing on the functional input, CRs receive both GABAergic and glutamatergic functional inputs, even though the latter have been found to be exclusively mediated via NMDA receptors<sup>26,27</sup>. In contrast, CR cell functional output has not been reported<sup>24,25</sup>. Even upon a broad optogenetic stimulation of neocortical CRs, Riva et al.<sup>28</sup> found no excitatory synaptic output responses onto layer 1 interneurons and no evoked local field potential in layer 2/3<sup>28</sup>. In summary, CRs are embedded in the developing mouse cortical circuit in a unique manner, despite their relatively short survival window. Specifically, CRs start to dissipate during the second postnatal week, a process largely completed by postnatal day (P) 14 in the barrel cortex (primary somatosensory cortex (S1)), which coincides with the start of active sensation via whisking<sup>6,26,28–30</sup>.

The mechanisms of CR cell death are still largely unknown, however, it has been shown that a subpopulation of CRs originating from the hem and septum (labeled by  $\Delta Np73$ ) is eliminated via *Bax*-dependent cell death<sup>26,31,32</sup>. Removal of *Bax* from these CRs leads to their survival, which is accompanied by an exuberance of dendrites and increase in spine density in layer 2/3 pyramidal cells, resulting in an excitation/inhibition imbalance<sup>28</sup>. CR cell-death and distribution appear to also be regulated by neural activity<sup>28,33</sup>. Specifically, NMDA-type glutamate receptors and excitatory GABAergic signaling regulate CRs distribution and promote their death, respectively, due to the sustained expression of the NKCC1 transporter<sup>33,34</sup>. Despite a handful of previous studies, it still remains unclear how the transient connections onto CRs contribute to cortical circuit formation and function.

Based on reported data, we hypothesized that CRs act as a developmental bridge between inhibitory and excitatory cortical cells, thereby regulating the development of inhibition in the cortex. Using mouse genetics, anatomical and functional approaches, we find that CRs receive GABAergic inputs mainly from layer 1 neurons and that their neonatal death leads to the proper development of inhibitory projections from layer 1 interneurons to layer 2/3 pyramidal cells. Using in vivo recordings and behavioral experiments, we show that this connectivity is crucial for the maturation of sensory-driven excitability within and especially across cortical columns, important for normal sensory stimulus discrimination. Hence, CR cell death is a key phenomenon for the development of sensory processing.

## Results

### Neocortical CRs mainly receive inputs from L1 GABAergic neurons

To assess the potential impact of CR cell death in the development of the cortical circuit, we first aimed to identify the circuit that CRs are part of. To achieve this in a comprehensive and unbiased manner, we utilized compound mouse genetics in combination with pseudo-typed rabies viral tracing (RV). We used the  $\Delta Np73^{Cre}$  mouse line ( $\Delta Np73^{Cre}Bax^{flox/+}$ -HTB) to trace the presynaptic partners of CRs deriving from Septum and Hem as they make up 70% of the total CRs population<sup>6</sup>. These heterozygous mice for *Bax* are used as Controls for our following conditional knock-out experiments, as they do not show any phenotypic difference compared to wild-type ( $\Delta Np73^{Cre}Bax^{+/+}$ ) animals<sup>6</sup>. The rabies virus is engineered to infect CRs that express eGFP along with the Avian receptor TVA and the G protein provided by the HTB mouse line. The RV spreads into first-order synaptically coupled neurons in the retrograde direction<sup>35</sup>. Direct presynaptic partners of CRs are fluorescently marked by mCherry expression and the primary infected cells (starter cells) are identified by double labeling of mCherry and nuclear eGFP (provided by the HTB line). The viral injections were performed at either P2 or P15 and the brains were

collected and analyzed at P5-7 or P21, respectively (Fig. 1a). Slightly different temporal windows for brain collection were used, since effort was made to inject as early as possible in neonatal mice and collect prior to the death of CRs, whereas this was not an issue for older animals. At both neonatal (P5-7) and young adult (P21) time points we found that the majority of presynaptic partners, normalized to the number of starter cells, in the  $\Delta Np73$ -expressing CRs are in L1, with few neurons located in deeper layers (Fig. 1bi-ii,c). We note that due to the very few surviving CRs in the older mice, it was more challenging to obtain similar numbers of animals for analysis between the two age groups ( $\geq 3$  mice). Nevertheless, our data shows that septum and hem-derived CRs that express  $\Delta Np73$  are mostly connected with L1 neurons.

Having revealed the major input onto CRs, we next aimed to manipulate the time window of CR cell survival in order to assess the impact of their death on the circuit they are embedded in. To achieve this, we conditionally (c) removed *Bax* in the  $\Delta Np73$ -fate mapped cells, which allows CRs to survive in the cortex into adulthood (*Bax* cKO:  $\Delta Np73^{Cre}Bax^{flox/flox}$ ), exceeding their apoptotic window<sup>6</sup>. First, we aimed to validate and characterize the *Bax* cKO mouse model in our region of interest, the barrel cortex (BC), at P5-7 and P21. The fate-mapping was performed by crossing the Control and *Bax* cKO mice with a tdTomato reporter mouse line (*Aii4*) to label CRs across their lifespan. To comprehensively quantify the density of CRs in the barrel cortex, we implemented a CLARITY-based tissue clearing protocol, followed by light-sheet microscopy using a custom-built microscope (mesoSPIM)<sup>36</sup>. The auto-fluorescence of the barrels allowed for the detection of the barrel cortex and enabled us to accurately localize and count CRs in the two genotypes. The analysis at P5-7 showed no significant difference in the number of L1 CRs between Control and *Bax* cKO mice (Supplementary Fig. 1a–d). However, at P21, the *Bax* cKO mice had significantly more CRs in the barrel cortex compared to Controls. This finding allowed us to use the third postnatal week to investigate how the cortical circuit would be affected by CRs survival (Supplementary Fig. 1e).

Immunolabeling for Prox1 on the P21 cortical slices of the *Bax* cKO confirmed that the surviving fate-mapped cells are CRs and not L1 inhibitory neurons (Suppl. Figure 1f). We additionally explored changes in the gross architecture of barrels, potentially caused by the CRs survival in the *Bax* cKO mice. There were no significant differences in barrel length, volume, and distance between B2-C2 barrels when comparing *Bax* cKO against Control mice (Supplementary Fig. 1g).

After the validation of the genetic manipulation, we proceeded to assess how the surviving CRs are embedded into the network, using the same pseudo-typed rabies viral approach as in Control mice. Our analysis showed that in the *Bax* cKO mice, the presynaptic partners of CRs are similar in numbers and location at both neonatal and later time points (Fig. 1biii-iv, d). Interestingly, the distribution of CR presynaptic partners in the *Bax* cKO at P21 seems to mimic the one in the Control at P5-7 (Fig. 1c). Young and surviving neocortical CRs receive their major input from L1 interneurons. The observed differences between L1 and L2/6 in Control P5-7 and *Bax* cKO P21 are not apparent when we compare the presynaptic partners across all layers at the two-time points (Supplementary Fig. 2a). Overall, young and surviving neocortical CRs are embedded into the circuit receiving their major input from L1 interneurons.

It is now well appreciated that besides CRs, which die early in development, adult L1 is solely occupied by GABAergic neurons<sup>37</sup>. To assess if the inputs that CRs receive from L1 across development are indeed GABAergic and functional, we performed in vitro whole-cell patch-clamp recordings from CRs after stimulation with an electrode in L1. An input-output protocol was implemented by increasing the stimulation intensity delivered in L1 (20–450  $\mu$ V) and measuring the evoked GABAergic postsynaptic currents. These currents for simplicity are referred to as evoked inhibitory postsynaptic currents (eIPSCs), even though they act as excitatory inputs on CRs based on cell-

attached recordings (Supplementary Fig. 2b–d). To make sure that pure GABAergic responses were recorded, we clamped the membrane potential at  $V_m = 0$  mV and blocked ionotropic glutamate receptors pharmacologically using CNQX and APV (Fig. 1e). Similar to the pseudo-typed rabies tracing experiments, the recordings in both Control and *Bax* cKO mice were performed during the first three postnatal weeks (P5–7, P11–13 and P21) focusing on the barrel cortex. At the end of the first postnatal week (Fig. 1f, g), the strength of GABAergic inputs to CRs in *Bax* cKO mice did not significantly differ from those recorded from the Control mice. At the intermediate time point (P11–13), the evoked GABAergic inputs showed a higher amplitude when the stimulation intensity was increased, but the two groups

did not differ significantly (Supplementary Fig. 2e, f). At P21, the surviving CRs in the *Bax* cKO showed responses similar to those in P11–P13 in Control and *Bax* cKO mice (Fig. 1g, Supplementary Fig. 2g), indicating the functional preservation of their inputs. Our anatomical and functional results show that CRs mainly receive functional connections from L1 GABAergic interneurons, which are enhanced with development and retained when CRs survive.

### Preventing CR cell death decreases L1 inhibition onto L2/3 pyramidal cells

It is known that a large population of L1 interneurons provides slow inhibition onto the apical dendrites of layer 2/3 pyramidal cells,

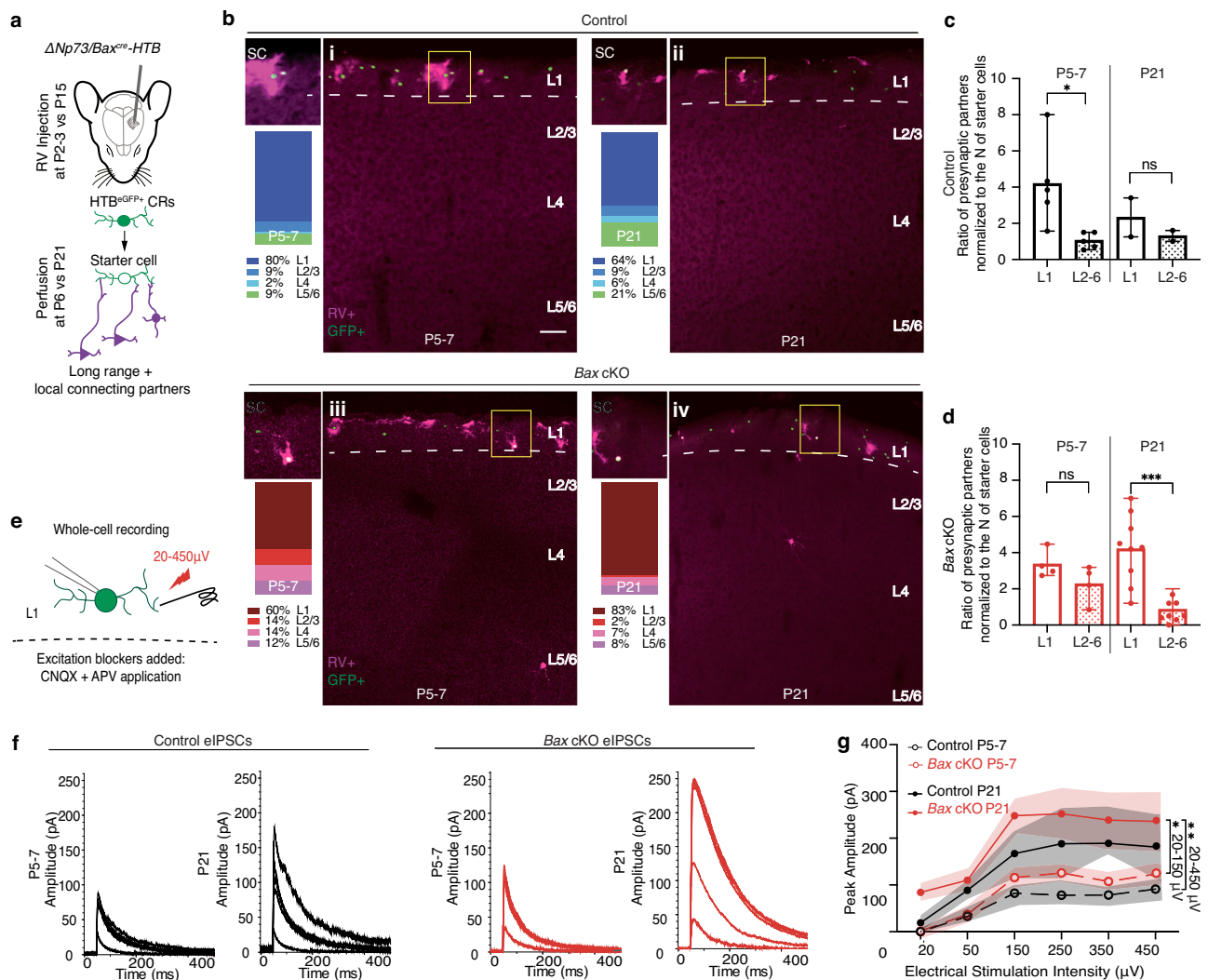


**Fig. 1 | Cajal-Retzius cells receive the bulk of their inputs from layer 1 GABAergic neurons.** **a** Schematic figure for anatomical tracing, targeting CRs. **bi-iv** Examples of stained presynaptic partners (magenta in place of mCherry) of CRs (green) and starter cells (white) for Control and *Bax* cKO mice at P5–7 (Control  $N = 5$ , *Bax* cKO  $N = 4$ ) and P21 (Control  $N = 2$ , *Bax* cKO  $N = 9$ ). Scale bar = 100  $\mu$ m. The layers have been standardized based on DAPI staining. The yellow boxes represent the zoomed in pictures of the starter cells (SC) on the left of each image. The boxes below the zoomed images show the percentage of presynaptic partners across layers. **c, d** One-way Anova was performed to compare the effect of CRs survival across development  $F(7,32) = 1.4$ ,  $p = 0.0002$  two-tailed. For each group all brain slices with starter cells and presynaptic partners were counted and averaged per brain (min 3 slices per brain). Data are presented as mean values  $\pm$  SD. **e** Schematic representation of the in vitro whole-cell patch-clamp recordings of CRs during electrical stimulation of L1. Increased stimulation (20–450  $\mu$ V) was performed in L1

and the evoked inhibitory postsynaptic currents (eIPSCs) of the patched CRs were measured upon CNQX and APV application at  $V_m = 0$  mV. **f** Average traces of inhibitory inputs received by CRs across groups and ages. **g** Multiple t-test (two-sided) analysis showed a significant difference between the Control CRs at P5–7 and the *Bax* cKO CRs at P21 across all stimulation paradigms. Using the same analysis a significant difference was observed for *Bax* cKO CRs at P5–7 vs P21 only for the initial stimulation paradigms (20–150  $\mu$ V). All groups at P5–7 have 6 cells/3 mice. At P21 the Control  $N = 2$  cells/2 mice and the *Bax* cKO  $N = 6$  cells/3 mice. Statistics could not be performed for the Control CRs at P21 since it was more challenging to obtain adequate numbers of mice for analysis (2 out of 6 patched mouse brains). Data are presented as mean values  $\pm$  SEM. The significance threshold was set to  $p < 0.05$ ; different degrees of significance are indicated by asterisks ( $p < 0.05$ ; \*,  $p < 0.01$ ; \*\*,  $p < 0.001$ ; \*\*\*, ns stands for non-significant result). Source data are provided as a Source Data file.



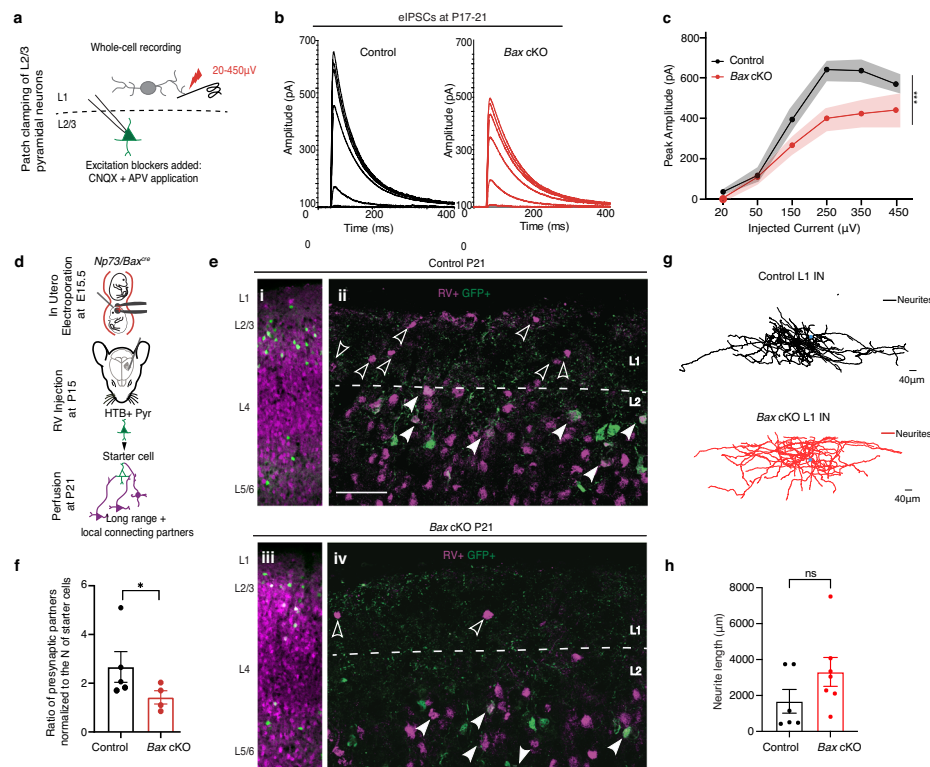


**Fig. 2 | Preventing Cajal-Retzius cell death affects the development of inhibitory connectivity onto layer 2/3 pyramidal cells.** **a** Schematic illustration of the in vitro whole-cell patch-clamp recordings of layer (L)2/3 pyramidal cells during electrical stimulation of layer (L)1. Increased stimulation intensity (20–450  $\mu$ V) was applied in L1 and the inhibitory postsynaptic currents of the patched neurons were measured upon glutamatergic transmission blocker (CNQX and APV) application at P17–21. **b** Average traces of evoked inhibitory post-synaptic currents (eIPSCs) received by L2/3 pyramidal neurons across groups. **c** Statistical comparisons of eIPSCs received by L2/3 pyramidal cells across groups using Mixed-Effects model (REML) (two-sided). At P17–21 (Control  $N=11$  cells/5 mice, Bax cKO  $N=10$  cells/5 mice) the groups differ significantly ( $F(5,50)=82.37$ ,  $P=0.0001$ ). There was also a significant difference between the interaction of group and stimulation intensity ( $F(5,37)=2.89$ ,  $P=0.0001$ ). Data are presented as mean values  $\pm$  SEM. **d** Schematic illustrating the procedure for anatomical tracing of the presynaptic partners of L2/3 pyramidal cells using pseudotyped rabies virus (RV). **e** i, iii: Examples of L2/3

pyramidal cells expressing the HTB plasmid (green), starter cells (white) and their presynaptic partners across layers (magenta in place of mCherry). ii, iv: Zoomed-in examples where the white arrows point to L2/3 starter cells infected by RV. The empty arrows point to L1 presynaptic partners of L2/3 pyramidal cells (magenta) in the Control and Bax cKO mice at P21 (Scale bar 100  $\mu$ m). The layers have been standardized based on dapi staining. **f** Ratio of presynaptic partners in L1. The ratios of the two groups (Control  $N=5$  mice, Bax cKO  $N=4$  mice) differ significantly (Mann–Whitney  $U=1.50$ ,  $P=0.03$  two-tailed). Data are presented as mean values  $\pm$  SEM. **g** Morphology of L1 interneurons at P16–25 for Control ( $N=6$  cells/4 mice) and Bax cKO ( $N=7$  cells/5 mice) mice. Blue dot denotes cell body location. **h** Quantification of neurite length and group comparisons using the Mann–Whitney  $U$  (two-tailed test) show no significant differences across groups. Data are presented as mean values  $\pm$  SEM. Significance threshold was set to  $p < 0.05$ ; different degrees of significance are indicated by asterisks ( $p < 0.05$ ;  $*p < 0.01$ ;  $**p < 0.001$ ;  $***$ , ns stands for non-significant result). Source data are provided as a Source Data file.

affecting cortical excitability during sensory plasticity<sup>38–40</sup>. Since CRs predominantly receive inputs from L1 GABAergic neurons, we subsequently explored whether their cell death is a key step for the establishment of inhibition from L1 interneurons onto L2/3 pyramidal cells.

To address this point, we performed whole-cell patch-clamp recordings from L2/3 pyramidal cells at P5–7, P11–13, and P17–P21 and recorded the evoked IPSCs upon the same electrical stimulation protocol (20–450  $\mu$ V) delivered in L1 as for CRs. Again, to ensure that we record pure evoked GABAergic responses (eIPSCs), we clamped the membrane potential at  $V_m=0$  mV and pharmacologically blocked ionotropic glutamate receptors using CNQX and APV (Supplementary Fig. 3a). At P5–7, L2/3 pyramidal cells in both Control and Bax cKO mouse lines displayed a similar small response to L1 inhibitory stimulation (Supplementary Fig. 3b, d). These inhibitory responses increased for both groups at P11–13 (Supplementary Fig. 3c, d). However, at P17–21, L2/3 pyramidal cells in Bax cKO mice showed significantly smaller response amplitude compared to Controls (Fig. 2a–c). Post-hoc comparisons revealed that the difference between the two groups became stronger as the amount of the delivered current increased (Fig. 2b, c). To test if this observation is unique for L1, we electrically stimulated (150  $\mu$ V) both in L1 and L2/3 consecutively, while recording L2/3 pyramidal cells (Supplementary Fig. 3e). No differences

were observed when stimulating L2/3 between Control and Bax cKO mice, showing that CRs survival affects specifically the L1 GABAergic inputs (Supplementary Fig. 3f, g). Interestingly, in Control mice, GABAergic inputs are stronger in CRs compared to L2/3 pyramidal cells at P5–7. This pattern is reversed at the P21 time window after CRs have died (Supplementary Fig. 3h–j). Our results highlight that in the Bax cKO mice, L2/3 pyramidal cells receive overall weaker inhibition from L1 compared to Control mice at P17–21.

To explore if this phenomenon is related to the synaptic strength or to a reduction in the number of L1 neurons that are connected to L2/3 pyramidal cells, we again made use of the pseudo-typed rabies virus. To target L2/3 pyramidal cells we expressed the pCAG-HTB and pCAG-GFP plasmids in these cells by *in utero* electroporation at embryonic day 15.5 (E15.5). Subsequently, we performed viral injections at P15 and after 7 days the brains were collected and analyzed at P21. We evaluated the number of connecting partners across layers in Control versus Bax cKO mice (Fig. 2d). Our analysis showed that there was a reduction of L1 presynaptic partners in the Bax cKO mice (Fig. 2e–iv, f). No major differences across the other layers were observed, which is consistent with our functional data (Supplementary Fig. 4a, b). It should be noted, however, that the analysis of deeper layer presynaptic partners is very challenging at the site of the injections.

The vast majority of L1 interneurons express the marker NDNF<sup>41</sup>. To assess if our rabies findings are due to a change in the numbers of cortical interneurons, rather than a change in connectivity, we performed in situ hybridization (ISH) against NDNF in Control and *Bax* cKO mice. Our analysis did not reveal a significant difference in NDNF neuron numbers between the two groups (Supplementary Fig. 4c, d). Additionally, in L1 a large fraction of SST+ interneuron axonal processes are found<sup>20,42,43</sup>. Hence, we also examined if the numbers of SST+ interneurons are affected by the CRs survival via ISH against SST. Our analysis showed no significant difference in the number of neurons expressing SST+ in the cortex either (Supplementary Fig. 4c, e). Finally, to have an overview of the possible changes in the general population of interneurons we performed a GAD1 ISH, observing no significant difference between the two groups (Supplementary Fig. 4c, f). The RV+ neurons in L1 were also GAD1+, however, it should be noted that performing immunohistochemistry or ISH on cells that have been infected with pseudo-typed rabies does not work optimally (Supplementary Fig. 4g, h).

To explore whether CRs survival could affect the axonal or dendritic growth of L1 interneurons which could potentially explain the differences in connectivity, we filled L1 interneurons with biocytin in vitro using a patch pipette and traced their projections post-hoc. No differences were observed when analyzing the neurite length or complexity (Fig. 2g, h, Supplementary Fig. 4i, j). Hence, when neo-cortical CRs do not go through cell death, the apical dendrites of L2/3 pyramidal cells receive weaker inhibition coming from fewer L1 interneurons (only after the beginning of whisking P14), since the connections of the latter remain onto the surviving CRs.

### CR cell death is key for the development of sensory-driven cortical activity

Having identified a circuit motif that requires CRs for its proper development, we next explored how the lack of maturation of L1 inhibition onto L2/3 pyramidal cells affects sensory-driven activity in vivo. To gain an overview of the effect of altered cortical excitability, we first performed wide-field calcium imaging during multi-whisker and single-whisker stimulation in Control and *Bax* cKO mice, by crossing the Snap25-GCaMP6s mouse line with the Control and *Bax* cKO mice. The global neuronal GCaMP6s expression allowed us to measure fluorescence signals representing activity in all cortical neurons. This permitted us to examine how sensory stimuli of multiple versus a single whisker engage the cortex. The paradigm was performed in neonatal (P5-7), and in juvenile mice (P17-21) when CRs will have undergone cell death in Control mice, in contrast to *Bax* cKO mice. A Sholl-like analysis (based on peak  $\Delta F/F_0$ ) was applied to calculate not only the maximum amplitude of fluorescence changes ( $\Delta F/F_0$ ) but also the distance the signal spreads upon multi-whisker and single-whisker stimulation (Fig. 3a, b). We found that upon multi-whisker stimulation, the  $\Delta F/F_0$  peak amplitude in the barrel cortex in both groups is similar in P5-7 mice. However, at P17-21, the *Bax* cKO mice show a greater activation, which also spreads farther since the fluorescent intensity is higher in more consecutive circles across the hemisphere (Fig. 3c, d, Supplementary movie 1-4). For single-whisker stimulation, there was no significant difference between the two groups across ages (Fig. 3e, f). Thus, the increased spread of activation observed at P17-21 upon CR survival in the *Bax* cKO group was specific for multi-whisker stimulation, perhaps indicating that proper L1 to L2/3 cell connectivity contributes to curbing the spread of excitation.

To further reveal the characteristics of this unique multi-whisker-induced overexcitation seen in the wide-field imaging, we inserted silicon probes in the barrel field (S1) and performed the same multi- and single-whisker stimulation paradigms in the juvenile developmental stage (Fig. 4). The average multi-unit activity (MUA) was calculated across three different layers (L2/3, L4 and L5), defined based on the local field

potential and current source density (see methods). To verify that the brain activity was recorded from the barrel cortex, post-hoc immunohistochemistry was performed on the recorded brains using Vglut2 staining, which labels the thalamocortical terminals and hence reveals the characteristic barrel structure. Only recordings from the principal barrel column were taken into account for this analysis (Fig. 4a). We found that multi-whisker stimulation evoked significantly more spikes in the *Bax* cKO mice compared to Controls. This effect was much more prominent for L2/3 compared to L4 and L5 (Fig. 4b). We then analyzed the firing rate in two different time points: at 0–100 ms, which represents the maximum evoked firing rate upon whisker stimulation, and at 250–350 ms, which is a later phase, before the activity returns to baseline. We observed that L2/3 shows an increased spike rate at both time points; this was also the case in L5, albeit to a lesser degree, but not in L4 (Fig. 4c). The response was not statistically different upon single-whisker stimulation, in agreement with the wide-field imaging results (Fig. 4d, e). This finding emphasizes that the observed overexcitation is more apparent in L2/3 and across cortical columns as it occurs only upon multi-whisker stimulation. Therefore, if CRs do not undergo cell death, the apical dendrites of L2/3 pyramidal cells receive less inhibition from L1, which results in a L2/3 over-excitation in vivo upon multi-whisker stimulation. This observation reveals that L1 interneurons participate in the development of lateral inhibition in the cortex.

We next investigated whether this overexcitation in L2/3 is directly associated with the function of L1 interneurons. To assess this, we manipulated the function of L1 interneurons in the *Bax* cKO mouse line, using a combined viral injection of either an excitatory DREADD (AAV-hM3Dq<sup>mcherry</sup> + AAV-Dlx<sup>cre</sup> virus) or an inhibitory DREADD (AAV-hM4D(Gi)<sup>mcherry</sup> + AAV-Dlx<sup>cre</sup> virus). The Dlx virus was co-injected in both cases to target specifically interneurons in the barrel cortex. The viruses were carefully injected in the superficial L1 in order to have minimal spillover in deeper layers at P11. After at least eleven days we performed silicon probe recordings during multi-whisker stimulation and assessed the spiking activity after vehicle or CNO subcutaneous injection in the adult *Bax* cKO mice (1-2 months old) (Supplementary Fig. 5a). These injections allowed us to record the effect of either exciting or suppressing L1 IN output when the maturation of L1 inhibition onto L2/3 pyramidal cells was stalled (Supplementary Fig. 5b). We found that exciting L1 interneurons in the *Bax* cKO did not have a significant effect across layers. This indicates that the impaired connectivity between L1 interneurons and L2/3 pyramidal cells cannot be rescued functionally; even when L1 interneuronal activity is boosted, it is not enough to decrease the overexcitation observed due to the CRs survival dependent structural changes (Supplementary Fig. 5c, e). On the other hand, when these L1 interneurons were silenced, L2/3 and to a lesser extent L4 showed an increase in the firing rate. This suggests that in the *Bax* cKO mice, when the few L1 interneurons connected to L2/3 pyramidal cells are inhibited, the system becomes even more excitable (Supplementary Fig. 5d, f). This effect was observed for both the early (0–100 ms) and the late (250–350 ms) spiking phase of L2/3 neurons (Supplementary Fig. 5f). Overall, these experiments suggest that the increased spiking activity of L2/3 cells upon CRs survival is a direct result of the changes in L1 connectivity and functional inhibition.

Our in vivo functional experiments highlight that the *Bax* cKO mice display increased sensory-driven cortical excitation in L2/3 at the temporal and spatial domain, which is in line with the reduction of the incoming inhibition these cells receive from L1, limiting lateral inhibition. We finally aimed to test if this phenomenon observed specifically in L2/3 has an impact in sensory processing.

### CR cell death contributes to the development of somatosensory discrimination

Layer 2/3 is an associative layer, critically involved in higher-order sensory information processing and learning<sup>44</sup>. It contains neurons

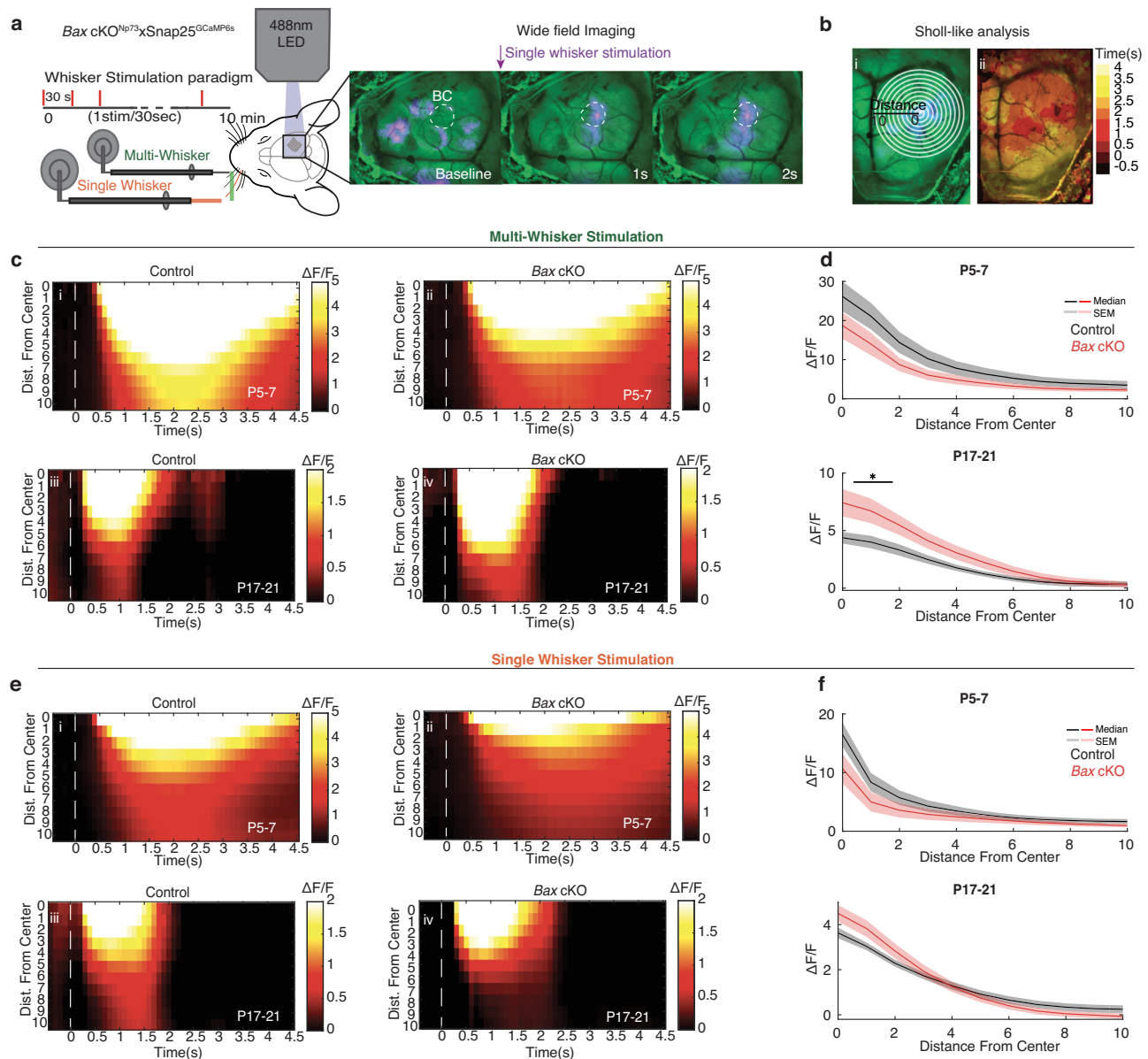


**Fig. 3 | Cajal-Retzius cell-survival increases the excitability of the cortex upon multi-whisker stimulation in vivo.** **a** Schematic representation of wide field (WF) calcium imaging in Control and *Bax* cKO mice during multi- and single-whisker stimulation. WF imaging (4.5 s per trial) has been performed across the left hemisphere in two different developmental stages in both mouse groups (P5-7: Control  $N = 6$  mice, *Bax* cKO  $N = 7$  mice, P17-21: Control  $N = 7$  mice, *Bax* cKO  $n = 7$  mice). **b** i: The  $\Delta F/F$  has been calculated and averaged for 20 trials. A Sholl-like analysis has been performed to calculate the maximum amplitude of fluorescence in 10 consecutive circles. ii: Example heat map of how fluorescence travels within the hemisphere over time after whisker stimulation. **c** Average  $\Delta F/F$  for each group over time based on the Sholl-like analysis for multi-whisker stimulation. **d**  $\Delta F/F$  group

comparisons for multi whisker stimulation at P5-7 and P17-21. At P17-21 there was a significant difference between the two groups. Statistics were calculated for each consecutive circle (1–10), (Mann–Whitney  $U_0 = 5$ ,  $P = 0.01$ ,  $U_1 = 4$ ,  $P = 0.007$ ,  $U_2 = 9$ ,  $p = 0.05$  two-tailed). Data are presented as median values  $\pm$  SEM. **e** Average  $\Delta F/F$  for each group over time based on the Sholl-like analysis for single whisker stimulation. **f**  $\Delta F/F$  group comparisons for single whisker stimulation at P5-7 and P17-21. There was no significant difference between the two groups. Data are presented as median values  $\pm$  SEM. The significance threshold was set to  $p < 0.05$ ; different degrees of significance are indicated by asterisks ( $p < 0.05$ ; \* $p < 0.01$ ; \*\* $p < 0.001$ ; \*\*\*, ns stands for non-significant result). Source data are provided as a Source Data file.

that receive inputs from both sensory and higher-order cortical areas, which are critical for integrating information across different brain regions<sup>43,45</sup>. In L2/3 of barrel cortex, pyramidal cell activity is critical for whisker-based object shape perception<sup>46</sup>. Despite previously published work, the role of L1 inhibitory cells in regulating the sensory-driven activity of L2/3 pyramidal cells and somatosensory processing is still not well understood. Our anatomical and functional experiments revealed that CR cell death mediates the maturation of L1 lateral inhibition onto L2/3 pyramidal cells. Prolonged CRs survival in the cortex impacts the early, but also late sensory-driven spiking activity of L2/3 pyramidal cells. CRs-mediated

development of inhibition therefore provides a good candidate for regulating the maturation of sensory processing. Hence, we next assessed how the maturational arrest of L1 to L2/3 connectivity upon CRs survival impacts whisker-based sensory discrimination. Adult Control ( $N = 8$ ) and *Bax* cKO ( $N = 7$ ) mice were trained in a Go/No-Go texture discrimination task<sup>47</sup>. A rough sandpaper (P100) served as ‘Go’ stimulus and a smoother sandpaper (P1200) as ‘No-Go’ stimulus. Go and No-Go trials were presented randomly with a 50% probability of each trial type, and with a maximum of three consecutive presentations of the same trial type (Fig. 5a). The mice used freely multiple whiskers to explore the different textures and learn the task.



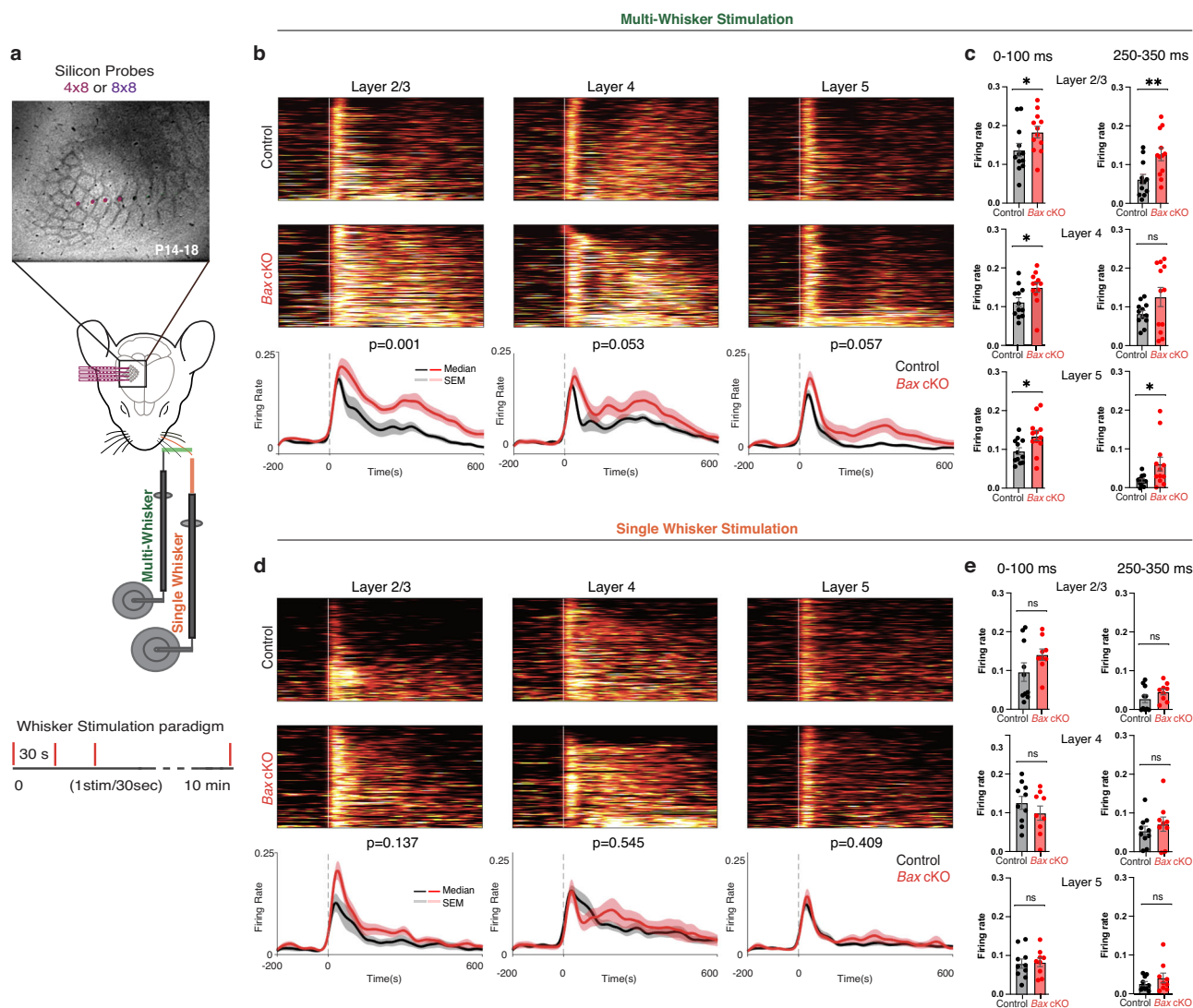


**Fig. 4 | Cortical layer 2/3 is majorly affected by Cajal-Retzius cell-survival showing increased excitability only upon multi-whisker stimulation.**

**a** Schematic representation of silicon probe insertion into the barrel field and trial protocol for multi- and single whisker stimulation at P14-18. VGlut2 stainings verified the probe insertion into the barrel field. Only probes within the barrels were chosen for the analysis. **b** Analysis for Multi-Whisker Stimulation: Raster plots showing firing rate and averaged Multi-Unit Activity in layer 2/3, layer 4, and layer 5 for all trials per mouse between groups. Statistics are calculated using the One-way ANOVA in order to compare the firing rate over time. **c** Histograms showing the average firing rate from 0–100 ms (peak) and 250–350 ms (late phase) (Control  $N=12$  barrels/ 5 brains, *Bax* cKO  $N=12$  barrels/5 brains). Statistics were calculated using the Mann-Whitney U test two-tailed (For 0–100 ms: Mann-Whitney  $U_{\text{layer2-3}}=27$ ,  $P=0.008$ ,  $U_{\text{layer4}}=34$ ,  $P=0.028$ ,  $U_{\text{layer5}}=36$ ,  $p=0.038$  two-tailed, for

250–350 ms: Mann-Whitney  $U_{\text{layer2-3}}=36$ ,  $P=0.038$ ,  $U_{\text{layer4}}=55$ ,  $P=0.34$ ,  $U_{\text{layer5}}=36$ ,  $p=0.039$  two-tailed). Data are presented as mean values  $\pm$  SEM. **d** Analysis for Single Whisker Stimulation: Raster plots showing firing rate and averaged Multi-Unit Activity in layer 2/3, layer 4 and layer 5 for all trials per mouse between groups. Statistics are calculated using the One-way ANOVA in order to compare the firing rate over time. **e** Histograms showing the average firing rate from 0–100 ms (peak) and 250–350 ms (late phase) (Control  $N=10$  barrels/ 5 brains, *Bax* cKO  $N=9$  barrels/5 brains). Statistics were calculated using the Mann-Whitney U test two-tailed. Data are presented as mean values  $\pm$  SEM. The significance threshold was set to  $p < 0.05$ ; different degrees of significance are indicated by asterisks ( $p < 0.05$ : \* $p < 0.01$ : \*\* $p < 0.001$ : \*\*\*; ns stands for non-significant result). Source data are provided as a Source Data file.

The training sessions (1 session per day) for each mouse lasted until they became experts, reaching a discriminability index ( $d'$ ) higher than 1.5. The expert mice performed the Go/No-Go task for a minimum of three consecutive days with stable performance using multiple whiskers. Then, all whiskers were trimmed except one (B2) and the mice performed for two consecutive days the same task using this single whisker (Fig. 5b) to assess the role of engaging lateral inhibition. Our results show that *Bax* cKO mice took significantly more days to learn the task (Fig. 5c), and showed lower expert performance level using multiple whiskers (Fig. 5d). Specifically, *Bax* cKO mice showed a significant drop in the 'Correct Rejection' trials accompanied by an increase of 'False alarm' trials using multiple whiskers

(Supplementary Fig. 6b, c). The Hit and Miss show no significant difference between the groups (Supplementary Fig. 6a, d). In contrast, and in agreement with in vivo functional results, when analyzing the performance of the animals using a single whisker, we observed no significant difference in the discriminability index between the two groups (Fig. 5e) nor in the task subcomponents (Supplementary Fig. 6e–h).

Overall, our findings support a prime role of CR cell death in the maturation of L1 lateral inhibitory control of L2/3 pyramidal cells during somatosensory discrimination and learning. Hence, the developmental cell death of CRs is a key event in the maturation of cognitive development.

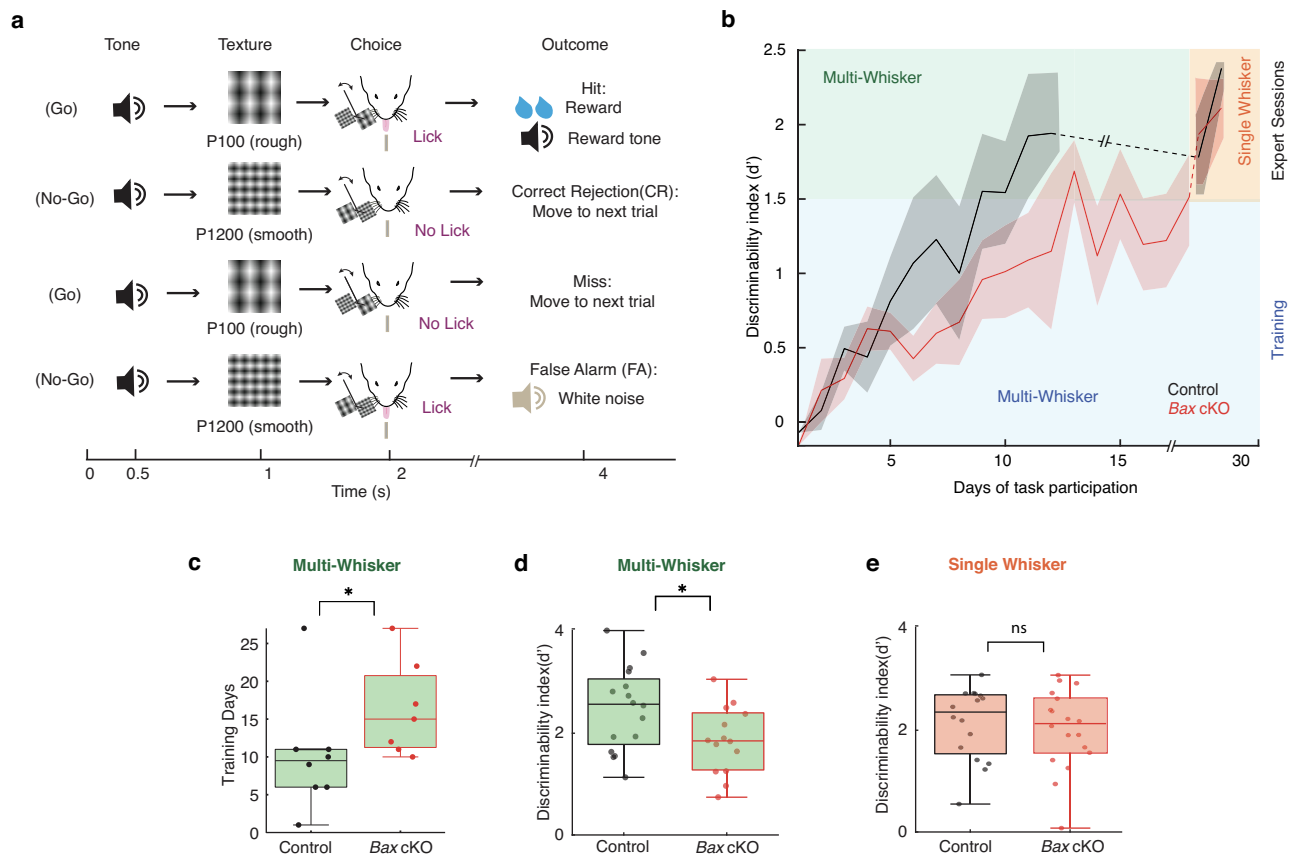


**Fig. 5 | Layer 2/3 increased excitability upon Cajal-Retzius cell-survival affects the tactile discrimination ability in the Bax cKO mice. a** Task design and trial structure of a Go vs No-Go texture discrimination task. After a trial-start tone, mice were trained to discriminate between a rough sandpaper (P100) which served as a target stimulus (Go) and a smoother sandpaper (P1200) served as non-target stimulus (No-Go). Sandpapers were mounted onto panels attached to a motorized linear stage which moved textures in and out of reach of whiskers. **b** Learning curves based on the  $d'$  of Control ( $N=8$ ) and Bax cKO ( $N=7$ ) mice. Expert level is defined as  $d' > 1.5$ , where  $d'$  is the sensitivity index of performance ( $d' = Z(\text{Hit}/(\text{Hit} + \text{Miss})) - Z(\text{FA}/(\text{FA} + \text{CR}))$ ). Data are presented as mean values  $\pm$  SEM. **c** Group comparison of training days in the task. The Bax cKO needed significantly more days to learn and complete the task (Control  $N=8$ , median = 8.5, Bax cKO  $N=7$ ,

median = 13.5, Mann-Whitney  $U=14$ ,  $P=0.03$  two-tailed). **d** Group comparison of  $d'$  for the two best expert sessions between groups for multi-whisker stimulation (Control  $N=16$  sessions/8mice, median = 2.57, Bax cKO  $N=14$  sessions/7mice, median = 1.85, Mann-Whitney  $U=63$ ,  $P=0.04$  two-tailed). **e** Group comparison of  $d'$  for the two sessions where a single whisker (B2) has been used. Mann-Whitney  $U$  two-tailed test was performed and no significant differences were observed (Control  $N=16$  sessions/8mice, Bax cKO  $N=14$  sessions/7mice). In the box plots the lower and upper boundaries of the box are the first and third quartiles, with the median annotated with a line inside the box. The whiskers extend to the maximum and minimum values. Significance threshold was set to  $p < 0.05$ ; different degrees of significance are indicated by asterisks ( $p < 0.05$ ;  $*p < 0.01$ ;  $**p < 0.001$ ;  $***$ , ns stands for non-significant result). Source data are provided as a Source Data file.

## Discussion

Although the role of developmental cell death in the formation and function of other body parts has been investigated, its impact on the formation of brain circuits is not understood. CRs are one of the two major transient neuronal populations in the cortex, with a reported critical prenatal role in cortical lamination through reelin secretion<sup>48</sup>. They are also embedded in cortical circuits postnatally, the importance of which had yet to be fully determined<sup>33,49,50</sup>.

In this study we find that L1 GABAergic interneurons provide a major input to CRs before the latter die. This transient connectivity is crucial for the establishment of mature L1 inhibitory connections onto L2/3 pyramidal cells. The timing of this event coincides with the transition from passive to active tactile exploration (whisking) in mice at P14 and the maturation of sensory-evoked responses in the barrel cortex<sup>51</sup>.

Preventing CR cell death leads to a developmental arrest of this L1 circuit, decreasing sensory-driven lateral inhibition, which results in an excess of late spiking activity of L2/3 pyramidal cells. The late spiking activity of L2/3 pyramidal cells has been shown to be important for sensory perception<sup>32,33</sup> and it is controlled by the delayed and slow inhibition that most of L1 GABAergic cells (expressing NDNF) provide onto pyramidal cells<sup>37,38</sup>. Our data show that the survival of CRs does

not only lead to enhanced activity of neurons in the principal barrel column but also to the engagement of a larger network, with activity spreading to neighboring barrels due to diminished lateral inhibition. This seems to lead to a stronger intermingling of sensory signals and loss of specificity and selectivity, explaining why the activity and sensory processing is affected in the multi-whisker paradigms and less so when a single whisker is used. Our data propose a mechanism by which L1 inhibitory cells migrating into the neocortex, first connect to CRs, until they and their future targets (L2/3 pyramidal cells) have developed sufficiently. Subsequently, L1 GABAergic cells may even contribute to the activity-dependent death of CRs in order to redirect their synapses onto the distal dendrites of pyramidal cells and begin engaging in higher-order computations upon active exploration.

Interestingly, the persistence of CRs has been revealed in post-mortem studies of probands with developmental disorders that relate to gyrification defects and developmental delay<sup>54</sup>. Furthermore, many neurodevelopmental disorders display sensory deficits, primarily related to over-excitability, which can lead to changes in sensory processing and even epilepsy<sup>55–57</sup>. Therefore, our findings could be of relevance for the etiology of these devastating and prevalent ailments.



Overall, our study uncovers how transient cortical cells and circuits can contribute to the formation of a mature network, which is key for cognitive development. This work opens the possibility that other distinct transient events and sub-circuits can drive the assembly of specific components of adult networks.

## Methods

### Animals

All animal experiments were approved by the Cantonal Veterinary Office Zurich and the University of Zurich. Animals were housed in a 12-h reverse dark-light cycle (7am to 7 pm dark) at 24°C at variable humidity. Animal lines used in this study are: The  $\Delta Np73^{Cre/RESGFP}$ <sup>58</sup> crossed with the  $Bax^{tm2Sjk};Bak^{1tm1Thsn}/J$  line<sup>59</sup> and is referred to as  $Bax$  cKO $^{\Delta Np73}$ . The  $Bax$  cKO $^{\Delta Np73}$  mouse line was crossed with Ai14 (B6.129S6-Gt(ROSA)26Sortm14(CAG-tdTomato)Hze/J) for fate mapping/clarity experiments, HTB (B6-Gt(ROSA)26Sortm1(CAGneo;HTB)Fhg)<sup>60</sup> for the pseudo-typed rabies viral tracing experiments, and with the B6.Cg-Snap25 $^{tm3.1Hze>/J}$  for the wide-field imaging. Littermates expressing  $\Delta Np73^{Cre}Bax^{flox/+}$  were used as Controls since heterozygous mice do not show any phenotypic difference compared to wild-type animals<sup>6</sup> and  $\Delta Np73^{Cre}Bax^{flox/flox}$  were used as experimental mice. All transgenic mice were kept in a C57BL/6J background. All experiments were performed on both sexes, except the behavioral experiments, which were performed only on males.

### Passive clearing, imaging, and cell counting

We performed passive clearing using a hydrogel-based tissue clearing method<sup>61,62</sup>. Briefly, the animals were deeply anesthetized by injecting Ketamine/Xylazine. The final dose for ketamine is 65 mg/kg (maximum injected volume is 10 ml/kg) and for Xylazine is 13 mg/kg (maximum injected volume is 10 ml/kg); the injection is done using an insulin syringe (30G $\frac{1}{2}$ ), intraperitoneally. We tested anesthesia levels with gentle foot pinches and waited for loss of motor response. Then the mice were transcardially perfused using 1x PBS and Hydrogel solution (1% PFA, 4% Acrylamide, 0.05% Bis). The collected brains were post-fixed for 48 h in a Hydrogel solution (1% PFA, 4% Acrylamide, 0.05% Bis). Afterwards, the Hydrogel polymerization was induced at 37 °C. Following the polymerization the brains were immersed in 40 mL of 8% SDS and kept shaking at room temperature (RT) until the tissue was cleared sufficiently (10–40 days depending on the animal age). Finally, after 2–4 washes in PBS, the brains were put into a self-made refractive index matching solution (RIMS)<sup>63</sup>. They were left to equilibrate in 5 mL of RIMS for at least 4 days at RT before being imaged. After clearing, brains were attached to a small weight and loaded into a quartz cuvette, then submerged in RIMS and imaged using a custom-built mesoscale selective plane illumination microscope (mesoSPIM)<sup>36</sup>. The microscope consists of a dual-sided excitation path using a fiber-coupled multiline laser combiner (405, 488, 515, 561, 594, 647 nm, Omicron SOLE-6) and a detection path comprising an Olympus MVX-10 zoom macroscope with a 1x objective (Olympus MVPLAPO 1x), a filter wheel (Ludl 96A350), and a scientific CMOS (sCMOS) camera (Hamamatsu Orca Flash 4.0 V3). For imaging tdTomato and eGFP, a 594 nm excitation with a 594 long-pass filter (594 LP Edge Basic, AHF) and 488 nm & 520/35 (BrightLine HC, AHF) were used respectively. The excitation paths also contain galvo scanners (GCM-2280-1500, Citizen Chiba) for light-sheet generation and reduction of streaking artifacts due to absorption of the light-sheet. In addition, the beam waist is scanning using electrically tunable lenses (ETL, Optotune EL-16-40-5D-TC-L) synchronized with the rolling shutter of the sCMOS camera. This axially scanned light-sheet mode (ASLM) leads to a uniform axial resolution across the field-of-view of 5–10  $\mu$ m (depending on zoom and wavelength). Field of views measure around 10.79 mm at x1 or x 0.8 magnification (Pixel size: 5.27  $\mu$ m) for overview datasets. Further technical details of the mesoSPIM are described elsewhere

([www.mesospm.org](http://www.mesospm.org)). The images generated with the mesoSPIM were preprocessed using Fiji and Imaris software to generate the images of the barrel cortex. For the quantification of neurons the collected RAW files were converted to HDF5 format and each z-plane was median filtered (window size 2 pixels) and convolved with a disc kernel (radius 1.5, convolution window size 10). The convolution was performed on the log-transformed z-plane and the convolution result was thresholded (threshold 0.3). On the convolved, thresholded z-planes local maxima were detected and then consolidated into cell detections in 3D space by matching and grouping detections on adjacent slices that are less than 5 pixels apart. Grouped detections were discarded if they spanned less than 4 adjacent slices. For the remaining grouped detections 3D cell positions were defined by the detection at median z location. 3D consolidated detections were filtered anatomically and morphologically using a semi-automated procedure to exclude non cortical detections and detections not corresponding to neurons (e.g. blood vessels). For the analysis Dataspace<sup>64</sup> was used: <https://github.com/skollmor/dspace>.

### In Utero electroporations

For the L2/3 pyramidal cell-tracing experiments, Control and  $Bax$  cKO embryos were co-electroporated with pCAG-HTB and pCAG-GFP plasmids at E15.5 in order to target the L2/3 pyramidal cells.

The *in utero* electroporations were performed as previously described<sup>65</sup>. Briefly, E15.5 pregnant mice were anesthetized using isoflurane, and a small cut (around 2 cm) was performed between the third and fourth pairs of mammary glands; the skin and the peritoneum were gently separated around the incision site; another vertical incision through the peritoneum was done to expose the abdominal cavity. Plasmids solution was injected into the lateral ventricle of embryo brains using a pulled glass capillary. 5 pulses at 45 V of 50 milliseconds spaced by 950 milliseconds were delivered. After electroporation, the embryos along with the embryonic chains were returned to the abdominal cavity; sterile warm saline solution was poured inside. The abdominal wall and the skin were sutured separately.

### Monosynaptic Rabies tracing injections

For the CRs-tracing experiments, the HTB reporter line was crossed with the  $Bax$  cKO mouse line. The mice were placed in an induction chamber and deeply anesthetized (O2 1 L/minute, isoflurane 3–5%). We tested anesthesia levels with gentle foot pinches and waited for loss of motor response. Then we transferred the mice on a heating pad and placed the snout into a face mask (O2 1 L/minute, isoflurane 1–4%). The concentration of isoflurane was adjusted according to the age and depth of anesthesia of the individual mouse.

Next, we injected at P2 or P15 the ASLV-A envelope glycoprotein (EnvA) pseudo-typed, glycoprotein-deleted rabies virus SADG-mCherry(EnvA)<sup>66</sup>. 200 nl of the virus were topically applied (15 nl/s) on top of the barrel field of primary somatosensory cortex (S1). The application was carried out using a glass micropipette attached to a Nanolitre 2010 pressure injection apparatus (World Precision Instruments).

For the L2/3 pyramidal-tracing experiments,  $Bax$  cKO embryos were co-electroporated with pCAG-HTB and pCAG-GFP plasmids at E15.5 in order to allow a sparse, but strong expression of the TVA receptor and the glycoprotein “G” in L2/3 pyramidal cells. At P15 the electroporated pups were injected in the barrel field of S1 with 200 nl (15 nl/s) of the pseudo-typed rabies virus using the same technique mentioned above.

After the surgeries, the animals were monitored and returned to their home-cage for maximum 7 days to allow for adequate viral expression. The mice were then deeply anesthetized by injecting Ketamine/Xylazine in order to be perfused. The final dose for ketamine is 65 mg/kg (maximum injected volume is 10 ml/kg) and for Xylazine is

13 mg/kg (maximum injected volume is 10 ml/kg); the injection is done using an insulin syringe (30 G $\frac{1}{2}$ ), intraperitoneally. We tested anesthesia levels with gentle foot pinches and waited for loss of motor response. We perfused the mice with 10 ml PBS followed by 15 ml 4% PFA and their brains were post-fixed for maximum 2 hours. The brains were cut with a vibratome (Leica) in 30  $\mu$ m-thick slices and then stained with antibodies (mCherry or GFP at concentration 1:500, Sigma-Aldrich) or were prepared for fluorescent In Situ Hybridization-ISH (GAD1, NDNF, SST).

### On slide histological experiments

As mentioned above, the brains of mice that were used for immunohistological or in situ hybridization experiments were fixed and sectioned.

For immunohistological experiments, sections were mounted on Superfrost Excell Microscope Slides (Eprelia 4941EXC-001), and left to dry for at least 1 hour, to ensure optimal adhesion. Subsequently, they were washed 3 times in 1x PBS for 5 min, followed by a 2-hour incubation in blocking solution (5% BSA, 10% NDS, 0.3% Triton X-100 in 1x PBS), after which primary antibodies were incubated at 4°C, overnight, in the same buffer. Primary antibodies used in such experiments were the following: chicken anti-GFP (Abcam ab13970, used at 1:1000), rabbit anti-mCherry (Invitrogen PA5-34974, used at 1:500), Guinea Pig anti-VGluT2 (Synaptic Systems 135404, used at 1:500) and rabbit anti-Prox1, c-terminal polyclonal (Abcam, ab76696, used at 1:500). The following day, sections were washed 3 times in 1x PBS containing 0.1% Triton X-100 for 5 min, incubated for 2 hours in blocking buffer containing any of the following secondary antibodies: donkey anti-chicken A488 (Jackson ImmunoResearch 703-545-155, used at 1:1000), donkey anti-rabbit Cy3 (Jackson ImmunoResearch 711-165-152, used at 1:1000) or donkey anti-Guinea Pig A488 (Jackson ImmunoResearch 706-545-148, used at 1:1000) and washed again 3 times in 1x PBS / 0.1% Triton X-100, and one last time in 1x PBS for 5 min. Finally, sections were mounted using DAPI-containing Fluoromount G (Southern Biotech 0100-20).

For in situ hybridization experiments, sections were again attached on glass slides, as mentioned above. After that, they were fixed in a 4% formaldehyde in 1x PBS solution for 10 min, washed twice in 1x PBS for 5 min, permeabilized in 1.5% H<sub>2</sub>O<sub>2</sub> in methanol for 15 min, washed twice in 1x PBS for 5 min, treated with 0.2 M HCl for 8 min, washed twice in 1x PBS for 5 min, digested with Proteinase K (10 mg/mL in 1x PBS) for 5 min, washed once in 1x PBS for 5 min, incubated in acetylation solution (1.33% triethanolamine, 0.06% HCl, 0.25% 0.5 mL acetic anhydride) for 10 min under gentle agitation, and finally, washed three times in 1x PBS for 5 min. Slides were then moved to a humid chamber and covered with hybridization solution (formamide 50%, 5x SSC, yeast tRNA 0.1 mg/mL, 1x Denhardt's solution, salmon sperm 0.1 mg/mL) for at least 2 h at room temperature, before being incubated overnight at 65°C with the same solution, containing RNA probes at a concentration of 1 ng/ $\mu$ L. The next day, the slides were washed once in 5x SSC for 5 min at 65°C, twice in 50% formamide / 2x SSC at 65°C for 30 min, once in 2x SSC at 37°C for 15 min, once in 0.1x SSC at 37°C for 15 min, and once in TN buffer (Tris-HCl 0.1 M, pH = 7.5 and NaCl 0.15 M). Slides were transferred again to the same humid chamber and incubated for 1 h in blocking solution (1x Maleic Acid Buffer, 2% blocking reagent (Roche), 0.3% Tween-20), before another overnight incubation at 4°C with anti-Dig-POD (Roche 11633716001, used at 1:500), goat anti-tdTomato (SICGEN Antibodies AB8181-200, used at 1:500) and rabbit anti-GFP (Invitrogen A-6455, used at 1:500), in the same blocking solution. On the third day, slides were washed in TNT buffer (TN buffer, 0.05% Tween-20) three times for 5 min and once for 1.5 h. Dig-RNA probes were fluorescently labelled with the TSA Plus Cy5 (Akoya biosciences NEL745001KT) or the TSA Plus Fluorescein (Akoya biosciences NEL741001KT) kits, according to the manufacturer's instructions, after which they were immediately washed 3

times in TNT buffer for 5 min, incubated with donkey anti-goat Cy3 (Jackson ImmunoResearch 705-165-147, used at 1:1000) and donkey anti-rabbit Alexa488 (Invitrogen A-11034, used at 1:1000) in blocking solution for 1.5 h, washed in TNT buffer three times for 5 min, and once more in TN buffer for 5 min, before mounting with DAPI-containing Fluoromount G.

GAD-1, NDNF and SST DIG-labelled probes were transcribed from P10 C57BL/6 J mouse brain cDNA, with the primers mentioned in the in situ hybridization atlases for each gene at <http://portal.brain-map.org/>.

The labelled neurons for each probe were counted by eye from three brains per group. Three slices depicting 1 hemisphere have been used and the counting was averaged per brain.

### Confocal imaging and image processing of rabies-traced tissue

All images from the injection sites were taken using a slide scanner (Zeiss Axio Scan.Z1) or a confocal microscope (Leica SP8) with a 10x (HC PL APO) or 20x (HC PL APO CS2) objective. Z-stacks of 0.5  $\mu$ m were taken with a resolution of 1600  $\times$  1600 pixels. Mosaic images of the injected hemisphere were taken. The obtained pictures were processed for analysis using the ZEN Software and Fiji. Pre- and post-synaptic RV-infected cells (expressing mCherry) in L2/3 and L1 were counted by eye. The ratio of rabies-infected cells per starter cell was calculated. The position of these cells in L1 was determined using Dapi staining. Slices with presynaptic cells but not starter cells were also included in the analysis.

### Neuron detection and segmentation in layer 2/3 rabies tracing data

We created custom algorithms using Matlab to detect neurons and find their laminar location as distance from pia (Suppl. Fig. 4a, Suppl. Table 1).

**Slice Edge Detection:** We have detected the edge of the L1 (pia) using custom-written computer vision algorithms by segmenting the image into two regions (structure vs empty) and fitting a partial circle at the edge of the slice.

**Neuron Detection:** First we detect all neuron-like objects using a LoG filter<sup>67</sup>. All detected points serve as centers of the candidate neurons. Each candidate neuron image (41  $\times$  41 pixel) is then fed into a 23-layer neural network to finalize their identity among three classes: Neuron, Dendrite or Noise. We have trained the detector using 1294 neurons, 369 dendrites, and 844 noise image patches using manual annotations from 16 coronal slices. The detector decides whether a candidate point is a neuron or not. We then assign the distance to pia value per neuron based on the Euclidean distance between the centroid of each neuron's soma to the top of the slice. Pixel space is converted to micrometers using the pixel size information at the end. The code generated for this analysis can be provided upon request.

### DREADD Injections

Adult mice underwent stereotaxic surgery to inject an inhibitory (ssAAV/2-hSyn1-dlox-hM4D(Gi)\_mCherry(rev)-dlox-WPRE-hGHp(A)) or an excitatory (ssAAV/2-hSyn1-dlox-hM3D(Gq)\_mCherry(rev)-dlox-WPRE-hGHp(A)) DREADD along with a DLX-cre expressing virus (ssAAV/2-hDlx-HBB-chI-hERT2\_Cre\_hERT2-WPRE-SV40p(A)) at a 1:1 ratio. Before the injections, the mice were placed in an induction chamber and deeply anesthetized (O2 1 L/minute, isoflurane 3-5%). We tested anesthesia levels with gentle foot pinches and waited for a loss of motor response. Then we transferred the mice on a heating pad and placed the snout into a face mask (O2 1 L/minute, isoflurane 1-3%). The concentration of isoflurane was adjusted according to the age and depth of anesthesia of the individual mouse. Subsequently, 200 nl of the viruses were co-applied (15 nl/s) on top of the barrel field of S1. The application was carried out using a glass micropipette attached to a

Nanolitre 2010 pressure injection apparatus (World Precision Instruments). The DREADD effects were tested using silicon probe recordings at least 11 days after surgery, to allow adequate viral-mediated protein expression.

### Acute Slice Electrophysiology

Whole-cell patch-clamp electrophysiological recordings were performed on L1 CRs and L2/3 pyramidal cells of the vS1 in acute slices. The mice were placed in an induction chamber and deeply anesthetized (O<sub>2</sub> 1 L/minute, isoflurane 3–5%). We tested anesthesia levels with gentle foot pinches and waited for a loss of motor response. Then the mice were decapitated and their brain was extracted and transferred to 4°C cooled physiological Ringer's solution (aCSF), of the following composition (μM): 125 NaCl, 2.5 KCl, 25 NaHCO<sub>3</sub>, 1.25 NaH<sub>2</sub>PO<sub>4</sub>, 1 MgCl<sub>2</sub>, 2 CaCl<sub>2</sub>, and 20 glucose. The brains were then glued to a stage and cut into 300 μm-thick coronal slices using a vibratome (VT 1200 S, Leica). The slices recovered in room temperature aCSF for 30 min before recording. The slices were then placed in the recording chamber of an upright microscope (Axioscope 2 FS, Zeiss) and superfused oxygenated (95% O<sub>2</sub> and 5% CO<sub>2</sub>) RT aCSF at a rate of 2–3 ml/min. The microscope was equipped with immersion differential interference contrast (DIA) and the following objectives were used to visualize the cells (10x/0.3, Olympus and 40x/0.8, Zeiss). A CMOS camera (optiMOS, QImaging) was attached to the scope to visualize the slice and cells through a computer screen. Patch pipettes were pulled from borosilicate glass capillaries (1.5 OD x 0.86 ID x 75 L mm, Harvard Apparatus) at a resistance of 3–4.5 MOhm. For recordings of electrically evoked currents, Clampex was used (v10.7.0.3, Molecular Devices 2016). The recording pipettes were filled with a solution containing the following (μM): 135 potassium D-gluconate, 4 NaCl, 0.3 Na-GTP, 5 Mg-ATP, 12 phosphocreatine-di-tris, 10 HEPES, 0.0001 CaCl<sub>2</sub> (pH 7.25, mOsm 290). In some cases 3 mg/ml biocytin (Tocris) was added in the recording solution. The electrical stimulator was positioned within L1 roughly 150 mm away from the patched L2/3 pyramidal neuron or the CR cell. Recordings were done in voltage clamp (V<sub>h</sub> = 0 mV), while 50 μM CNQX (Cat. Nr. 1045, Tocris) and 50 μM AP5 (Cat. Nr. 0106, Tocris) blockers were added to allow us to measure evoked GABAergic/inhibitory currents without contamination from ionotropic glutamate receptor-mediated currents. 20 μM of Gabazine (SR 95531 hydrobromide, Cat. Nr. 1262, Tocris) was added at the end of the recordings to verify that only GABAergic currents were measured. All pharmacology was washed in for at least 10 min before recording. Currents were evoked within the patched cells through the electrical stimulator. Access resistance was constantly monitored to ensure the quality and stability of the recording. The recorded data were included in the analysis only if the initial series resistance was less than or equal to 25 MOhm and did not change by more than 20% throughout the recording period. No compensation was made for the pipette and cell capacitance. The recorded data was sampled at 5 kHz.

### Patched cell reconstruction

In the cases where the patched cells needed to be reconstructed for morphological analysis, the experiments were performed as described below:

Firstly, biocytin (Tocris #3349) was added to the intracellular solution of the patch pipette (25 μg in 1 ml). After recording, the slices were fixed in 4% PFA overnight in 24-well plates, under gentle agitation.

Subsequently, free-floating immunofluorescent labelling of these sections was performed as follows: they were first washed 3 times in 1x PBS for 15 min, and incubated with Streptavidin-Alexa 555 diluted at 1:250 in PBS-0.25% Triton X-100, for 48 h, at 4°C. The slices were then washed again 3 times in 1x PBS-0.1% Triton X-100 for 15 min, before mounted on Superfrost slides (inside a well made from tape) with Vectashield (Vector Laboratories H-1000), and sealed with nail polish.

The cells were then imaged on a Leica SP8 confocal microscope, as described above.

The biocytin-filled patched cells were manually reconstructed, using the SNT plugin in Fiji/ImageJ, and the traces were analyzed with the built-in analysis pipeline of the plugin<sup>68–70</sup>.

### Animal surgery for wide-field imaging and multielectrode recordings

Mice were lightly anesthetized with urethane (the final concentration is 1 g/kg mouse weight for P6–7 mice, 1–1.25 g/kg for P14–P21 mice) throughout the whole experiment. A heating pad was used to maintain the mouse body temperature at 37 °C. The depth of anesthesia was checked with breathing rate and paw reflexes throughout the experiment. If the respiratory rate was slower than 3 times every 2 s, as measured by eye, the mouse or session would be considered as deeply anesthetized and would be excluded from the analysis. Then, the skull of the right hemisphere was exposed by removing the skin on top, and a metallic head plate was attached on the skull with cyanoacrylate glue and dental cement. For the wide-field experiments: after the skull exposure, a few drops of 1% agarose in ringer were applied on the head plate and the gel was secured with a glass square placed on top in order to have good resolution of the fluorescent activity upon wide field imaging. For the silicon probe experiments: A 20G needle was used to open a 2×2 mm cranial window, which exposed the barrel cortex. Extreme care was taken not to cause damage or surface bleeding in pups.

### Whisker evoked stimulation

Multiple or single whiskers were deflected 1 mm away from the whisker pad using a miniature solenoid actuator adapted from Krupa et al.<sup>71</sup>, driven by a stimulus generator (STG4002-160 mA, Multi Channel Systems MCS GmbH) connected with an in-house 10x voltage amplifier. The stimulator generated a 1000 mm displacement for 10 ms in the antero-posterior direction. Recordings were carried out while whiskers contralateral to the recording site were deflected. The stimulus takes 26 ms to reach the maximal 1 mm whisker displacement, with a total duration of 60 ms until it reaches baseline<sup>72</sup>. Per paradigm, single deflections were carried out at an inter-stimulus interval of 20 seconds, for 20 repetitions.

### Wide field imaging and analysis

Using the B6.Cg-Snap25<sup><tm3.1Hze>/J</sup> mouse line in combination with others, we shined blue light (488 nm LED) on the cortical surface and revealed the functional maps in the barrel cortex by stimulating multiple whiskers. Images were acquired through a 0.5× Nikon objective with a CCD camera with 5 or 10 frames per second (fps). The recordings lasted 10 s with a 2 s baseline and 8 s poststimulation period. After imaging, the mice were euthanized.

Wide-field calcium imaging data were analyzed using a custom-made MATLAB script (2019a, The MathWorks). The fluorescence change ( $\Delta F/F_0$ ) was calculated as the change of fluorescence intensity ( $\Delta F = F - F_0$ ) in each pixel divided by the baseline fluorescence intensity ( $F_0$ , average of 500 ms absolute fluorescence before the onset of whisker deflection) in the same pixel. The barrel cortex evoked activity over different age groups was compared by using the highest evoked calcium response. For the functional Sholl analysis, using the peak fluorescent change after whisker stimulation per mouse as the starting point in time and space, the average fluorescence line profile of every consecutive concentric circle (10 in number) was calculated, again as  $\Delta F/F_0$ . The code generated for this analysis can be provided upon request.

### In vivo multi-electrode silicon probe recordings and analysis

Neural activity was recorded with an 8 shank 64-channel 'silicon probe', inserted perpendicularly into vS1 (8×8-Edge-5mm-100-200-177, NeuroNexus Technologies or 4×8). Each of the shanks (5 mm long, of which



the 750 mm tip contained the recording sites) contained 8 recording sites (177 mm<sup>2</sup> surface area per recording site) spaced 100 µm apart. The distance between each shank was 200 µm. For all animals, the probe insertion points were marked by impregnating the probes with Dil (Cat. No. D282, Molecular Probes) before insertion. A silver wire placed over the cerebellum served as a ground electrode. All data were continuously digitized at 20 kHz and stored for offline analysis using 48- or 64-channel extracellular recording system (SC2x 32 and a 100-1-500 SN. 127, Multi Channel Systems MCS GmbH) and MC RACK software (Multi Channel Systems MCS GmbH). One hour following electrode insertion the recordings were started. For the experiments using DREADDS the electrical signals were recorded 1 hour after vehicle or Clozapine N-Oxide (CNO) sub-cutaneous injections. We performed the same stimulation protocol (single or multiple whiskers) for 20 trials. In all cases the total duration of the multi-electrode recordings varied between 3 and 5 h. After the recordings, mice were euthanized, perfused with PBS and the brains were post-fixed in 4% PFA for 2 hours for post-hoc immunohistochemical analysis with a VGlut2 antibody.

The extracellular silicon probe data were analyzed using a custom-made MATLAB script (2019a, The MathWorks) after converting the recorded.mcs files into.h5 format using Multi Channel Data Manager. The raw signal was bandpass filtered (0.8-5 kHz) and the multi-unit activity (MUA) was extracted using five different thresholds (3.5, 4, 4.5, 5, 5.5) multiplied by the standard deviation of the baseline for each genetic or chemogenetic condition. We have used thresholds that present the closest baseline firing rates between the conditions. We also wanted not to use trials in which the cortex is already active as a baseline. To accomplish that, we have only used trials that do not have significantly high baseline firing rates at the time of the corresponding whisker stimulation trial (we have 20 whisker-stimulation trials per barrel).

The current source density (CSD) map was used to identify L2-3, L4, and L5. The earliest CSD sink was identified as layer 4, followed by L2-3 and L5<sup>73,74</sup>. The MUAs were separated, and the average MUAs were calculated and smoothed by 5 or 10 ms sliding window averaging for each stimulation paradigm. The mean firing rate was calculated (0-100 ms and 250-350 ms after onset of whisker deflection) after averaging all the deflection trials. The code generated for this analysis can be provided upon request.

### Chronic cranial plate implantation and habituation

To allow long-term fixation of the mice in the behavioral set-up a head plate was placed in mice 10 days before the beginning of the behavioral testing. A metallic post for head fixation was implanted on the skull, using dental acrylic. Ten days after chronic window implantation, mice were handled daily for 1 week, while they became acclimated to a minimum of 15 min of head fixation.

### Texture-discrimination task

Behavioral experiments were performed using a data acquisition interface (USB-6008; National Instruments) and custom-written LabVIEW software (National Instruments) to control devices required for the task and for recording trial and licking data. Licking of a water port mounted to a piezo film sensor (MSP1006-ND; Measurement Specialties) triggered delivery of water (5 to 6 µl) through a miniature rocker solenoid valve (0127; Buerkert). The task was performed based on a previous study<sup>47</sup>. Briefly, mice were initially trained during two sessions to trigger water reliably by licking the lick port, and then progressed to the Go/No-Go task training. For texture discrimination, commercial-grade sandpaper (3 M) was used. Rough sandpaper (P100) served as a target stimulus and smoother sandpaper of (P1200) served as non-target stimulus. Sandpapers were mounted onto panels attached to a stepper motor (T-NM17A04; Zaber) and mounted onto a motorized linear stage (T-LSM100A; Zaber) to move textures in and out of reach of whiskers. This linear stage was mounted onto a pneumatic linear slider (SLS-10-30-P-A

Mini slide; Festo) to bring the sandpapers in and out of reach of the whiskers rapidly. Go and No-Go trials were presented randomly with a 50% probability of each trial type, and with a maximum of three consecutive presentations of the same trial type. A trial consisted of a “trial-start” auditory tone of 2000 Hz, a 0.5 second pre-stimulus period, a subsequent 1-second texture presentation period, and a choice window. Licking after target stimulus presentation and during choice window was scored as a ‘hit’, and triggered immediate water delivery along with a reward tone of 2000 Hz. When there was no lick, this was scored as a ‘miss’. After the presentation of non-target stimuli, a no-lick response was scored as a ‘correct rejection’, and licking was scored as a ‘false alarm’, where a 2-second white noise was delivered. A sensitivity index of animal performance ( $d'$ ) was calculated for all trials per session as  $d' = Z(\text{Hit}/(\text{Hit} + \text{Miss})) - Z(\text{FA}/(\text{FA} + \text{CR}))$ , where Hit and Miss are the numbers of hits and misses, respectively, CR is the number of correct rejections, FA is the number of false alarms.  $Z(p)$ ,  $p \in [0,1]$  is the inverse of the cumulative Gaussian distribution, where  $p$  is  $\text{Hit}/(\text{Hit} + \text{Miss})$  or  $\text{FA}/(\text{FA} + \text{CR})$ . Experimental sessions were considered for the analysis once animals reached a performance level of  $d' > 1.50$  for one session. All training and experimental sessions occurred once per day.

The drop of motivation of mice could be reflected as higher miss rate, therefore biasing the estimation of performance level. To ensure an accurate estimation of behavioral performance, we divided each session into sub-sessions of 50 trials, detected the first sub-session where the miss rate was above 20%, and excluded all following sub-sessions. Typically, this led to a total 50-200 trials per session. To quantify the behavioral performance, we calculated the overall performance level, defined as  $\text{Performance} = (\text{Hit} + \text{CR})/(\text{Hit} + \text{CR} + \text{FA} + \text{Miss})$ . Additionally, we also computed the hit rate as  $\text{Hit}/(\text{Hit} + \text{Miss})$ , the CR rate as  $\text{CR}/(\text{FA} + \text{CR})$ , the FA rate as  $\text{FA}/(\text{FA} + \text{CR})$ , and the miss rate as  $\text{miss}/(\text{Hit} + \text{Miss})$ . Statistics were done by pooling the top two sessions for multi and single-whisker stimulation sorted by  $d'$  for each mouse. The code generated for this analysis can be provided upon request.

### Statistical analysis

Data represented as averages  $\pm$  S.E.M. unless otherwise stated. Statistical comparisons were carried out by using a two-tailed Mann-Whitney U test for non-paired data. When data were normally distributed a t-test was performed. For the input-output analysis of the evoked stimulation in vitro, Repeated Measures ANOVA was performed. Significance threshold was set to  $p < 0.05$ ; in the figures, different degrees of evidence against the null hypothesis are indicated by asterisks ( $p < 0.05$ : \* $p < 0.01$ : \*\* $p < 0.001$ : \*\*\*).

### Reporting summary

Further information on research design is available in the Nature Portfolio Reporting Summary linked to this article.

### Data availability

The raw data generated in this study can be provided upon request. Source data are provided with this paper.

### Code availability

The code generated in this study can be provided upon request.

### References

1. Fuchs, Y. & Steller, H. Programmed cell death in animal development and disease. *Cell* **147**, 742–758 (2011).
2. Ghose, P. & Shaham, S. Cell death in animal development. *Development* **147**, dev191882 (2020).
3. Oppenheim, R. W. Cell death during development of the nervous system. *Annu Rev. Neurosci.* **14**, 453–501 (1991).
4. Maxwell Cowan, W., Fawcett, J. W., O'Leary, D. D. M. & Stanfield, B. B. Regressive events in neurogenesis. *Science* **225**, 1258–1265 (1984).

5. Wong, F. K. et al. Serotonergic regulation of bipolar cell survival in the developing cerebral cortex. *Cell Rep.* **40**, 111037 (2022).
6. Ledonne, F. et al. Targeted inactivation of bax reveals a subtype-specific mechanism of Cajal-Retzius neuron death in the postnatal cerebral cortex. *Cell Rep.* **17**, 3133–3141 (2016).
7. Wong, F. K. et al. Pyramidal cell regulation of interneuron survival sculpts cortical networks. *Nature* **557**, 668–673 (2018).
8. Sreenivasan, V. et al. Input-specific control of interneuron numbers in nascent striatal networks. *Proc. Natl Acad. Sci. USA* **119**, e2118430119 (2022).
9. y Cajal, S. R. *Comparative Study of the Sensory Areas of the Human Cortex*. (Clark University, 1899).
10. Retzius, G. DieCajal'schen Zellen der Grosshirnrinde beim Menschen und bei Saugetireren. *Biol. Untersuch.* **5**, 1–9 (1893).
11. Bielle, F. et al. Multiple origins of Cajal-Retzius cells at the borders of the developing pallium. *Nat. Neurosci.* **8**, 1002–1012 (2005).
12. Anstötz, M. & Maccaferri, G. A toolbox of criteria for distinguishing Cajal-Retzius cells from other neuronal types in the postnatal mouse hippocampus. *eNeuro* **7**, (2020).
13. Gesuita, L. & Karayannis, T. A 'Marginal' tale: the development of the neocortical layer 1. *Curr. Opin. Neurobiol.* **66**, 37–47 (2021).
14. Barber, M. & Pierani, A. Tangential migration of glutamatergic neurons and cortical patterning during development: Lessons from Cajal-Retzius cells. *Dev. Neurobiol.* **76**, 847–881 (2016).
15. de Frutos, C. A. et al. Reallocation of olfactory Cajal-Retzius cells shapes Neocortex architecture. *Neuron* **92**, 435–448 (2016).
16. Griveau, A. et al. A novel role for Dbx1-derived Cajal-Retzius cells in early regionalization of the cerebral cortical neuroepithelium. *PLoS Biol.* **8**, e1000440 (2010).
17. Ogawa, M. et al. The reeler gene-associated antigen on Cajal-Retzius neurons is a crucial molecule for laminar organization of cortical neurons. *Neuron* **14**, 899–912 (1995).
18. Ogino, H. et al. The secreted glycoprotein reelin suppresses the proliferation and regulates the distribution of oligodendrocyte progenitor cells in the embryonic neocortex. *J. Neurosci.* **40**, 7625–7636 (2020).
19. Vilchez-Acosta, A. et al. Specific contribution of Reelin expressed by Cajal-Retzius cells or GABAergic interneurons to cortical lamination. *Proc. Natl Acad. Sci. USA* **119**, e2120079119 (2022).
20. Cocas, L. A. et al. Cell type-specific circuit mapping reveals the presynaptic connectivity of developing cortical circuits. *J. Neurosci.* **36**, 3378–3390 (2016).
21. Kirischuk, S., Luhmann, H. J. & Kilb, W. Cajal-Retzius cells: Update on structural and functional properties of these mystic neurons that bridged the 20th century. *Neuroscience* **275**, 33–46 (2014).
22. Kirmse, K., Neuroscience, S. K.-J. of & 2006, undefined. Ambient GABA constrains the strength of GABAergic synapses at Cajal-Retzius cells in the developing visual cortex. *Soc. Neurosci.* <https://doi.org/10.1523/JNEUROSCI.0589-06.2006> (2006).
23. Soda, T. et al. Segregation and Coactivation of Developing Neocortical Layer 1 Neurons. *J. Neurosci.* **23**, 6272–6279 (2003).
24. Anstötz, M. et al. Morphology, input-output relations and synaptic connectivity of Cajal-Retzius cells in layer 1 of the developing neocortex of CXCR4-EGFP mice. *Brain Struct. Funct.* **219**, 2119–2139 (2014).
25. Radnikow, G., Feldmeyer, D. & Lübke, J. Axonal projection, input and output synapses, and synaptic physiology of Cajal-Retzius cells in the developing rat neocortex. *J. Neurosci.* **22**, 6908–6919 (2002).
26. Derer, P. & Derer, M. Cajal-retzius cell ontogenesis and death in mouse brain visualized with horseradish peroxidase and electron microscopy. *Neuroscience* **36**, 839–856 (1990).
27. Marín-Padilla, M. Cajal-Retzius cells and the development of the neocortex. *Trends Neurosci.* **21**, 64–71 (1998).
28. Riva, M. et al. Activity-dependent death of transient Cajal-Retzius neurons is required for functional cortical wiring. *elifesciences.org* <https://doi.org/10.7554/eLife.50503> (2019).
29. Price, D. J., Aslam, S., Tasker, L. & Gillies, K. Fates of the earliest generated cells in the developing Murine Neocortex. *J. Comp. Neurol.* **377**, 414–422 (1997).
30. Del Rio, J. A., Martinez, A., Fonseca, M., Auladell, C. & Soriano, E. Glutamate-like immunoreactivity and fate of cajal-retzius cells in the murine cortex as identified with calretinin antibody. *Cereb. Cortex* **5**, 13–21 (1995).
31. Ma, J., Yao, X. H., Fu, Y. & Yu, Y. C. Development of layer 1 neurons in the mouse neocortex. *Cereb. Cortex* **24**, 2604–2618 (2014).
32. Chowdhury, T. G. et al. Fate of Cajal-Retzius neurons in the postnatal mouse neocortex. *Front. Neuroanat.* <https://doi.org/10.3389/NEURO.05.010.2010/FULL> (2010).
33. Genescu, I. et al. Dynamic interplay between thalamic activity and Cajal-Retzius cells regulates the wiring of cortical layer 1. *Cell Rep.* **39**, 110667 (2022).
34. Blanquie, O., Liebmann, L., ... C. H.-C. & 2017, undefined. NKCC1-mediated GABAergic signaling promotes postnatal cell death in neocortical Cajal-Retzius cells. *academic.oup.com*.
35. Wickersham, I. R., Finke, S., Conzelmann, K. K. & Callaway, E. M. Retrograde neuronal tracing with a deletion-mutant rabies virus. *Nat. Methods* **4**, 47–49 (2006).
36. Voigt, F. F. et al. The mesoSPIM initiative – open-source light-sheet microscopes for imaging cleared tissue. *Nat. Methods* **16**, 1105 (2019).
37. Schuman, B. et al. Four unique interneuron populations reside in neocortical layer 1. *J. Neurosci.* **39**, 125–139 (2019).
38. Tamás, G., Lörincz, A., Simon, A. & Szabadics, J. Identified sources and targets of slow inhibition in the neocortex. *Science* **299**, 1902–1905 (2003). 1979.
39. Wozny, C. & Williams, S. R. Specificity of synaptic connectivity between layer 1 inhibitory interneurons and Layer 2/3 pyramidal neurons in the rat neocortex. *Cereb. Cortex* **21**, 1818–1826 (2011).
40. Abs, E. et al. Learning-related plasticity in dendrite-targeting Layer 1 Interneurons. *Neuron* **100**, 684–699.e6 (2018).
41. Webster, J. F., Vroman, R., Beerens, S., Sakata, S. & Wozny, C. NDNF is selectively expressed by neocortical, but not habenular neurogliaform cells. *Eur. J. Neurosci.* **53**, 3561–3575 (2021).
42. Tremblay, R., Lee, S. & Rudy, B. GABAergic interneurons in the neocortex: From cellular properties to circuits. *Neuron* **91**, 260 (2016).
43. Pakan, J. M. P. et al. Behavioral-state modulation of inhibition is context-dependent and cell type specific in mouse visual cortex. *Elife* **5**, e14985 (2016).
44. Larkum, M. A cellular mechanism for cortical associations: An organizing principle for the cerebral cortex. *Trends Neurosci.* **36**, 141–151 (2013).
45. Letzkus, J. J. et al. A disinhibitory microcircuit for associative fear learning in the auditory cortex. *Nature* **480**, 331–335 (2011).
46. Rodgers, C. C. et al. Sensorimotor strategies and neuronal representations for shape discrimination. *Neuron* **109**, 2308–2325.e10 (2021).
47. Chen, J. L., Carta, S., Soldado-Magraner, J., Schneider, B. L. & Helmchen, F. Behaviour-dependent recruitment of long-range projection neurons in somatosensory cortex. *Nature* **499**, 336–340 (2013).
48. Elorriaga, V., Pierani, A. & Causseret, F. Cajal-retzius cells: Recent advances in identity and function. *Curr. Opin. Neurobiol.* **79**, 102686 (2023).
49. Anstötz, M., Lee, S. K. & Maccaferri, G. Glutamate released by Cajal-Retzius cells impacts specific hippocampal circuits and behaviors. *Cell Rep.* **39**, 110822 (2022).
50. Anstötz, M., Lee, S. K., Neblett, T. I., Rune, G. M. & Maccaferri, G. Experience-Dependent Regulation of Cajal-Retzius Cell Networks in

- the Developing and Adult Mouse Hippocampus. *Cereb. Cortex* **28**, 672–687 (2018).
51. Cai, L. et al. Identification of a developmental switch in information transfer between Whisker S1 and S2 Cortex in Mice. *J. Neurosci.* **42**, 4435–4448 (2022).
  52. Sachidhanandam, S., Sreenivasan, V., Kyriakatos, A., Kremer, Y. & Petersen, C. C. H. Membrane potential correlates of sensory perception in mouse barrel cortex. *Nat. Neurosci.* **16**, 1671–1677 (2013).
  53. Libet, B., Alberts, W. W., Wright, E. W. & Feinstein, B. Responses of human somatosensory cortex to stimuli below threshold for conscious sensation. *Science* **158**, 1597–1600 (1967).
  54. Eriksson, S. H. et al. Persistent reelin-expressing Cajal–Retzius cells in polymicrogyria. *Brain* **124**, 1350–1361 (2001).
  55. Fritschy, J. M. Epilepsy, E/I balance and GABAA receptor plasticity. *Front Mol. Neurosci.* **1**, 5 (2008).
  56. Seneviratne, U., Cook, M. J. & D’Souza, W. J. Electroencephalography in the diagnosis of genetic generalized epilepsy syndromes. *Front Neurol.* **8**, 499 (2017).
  57. Canitano, R. Epilepsy in autism spectrum disorders. *Eur. Child Adolesc. Psychiatry* **16**, 61–66 (2007).
  58. Tissir, F. et al. DeltaNp73 regulates neuronal survival in vivo. *Proc. Natl Acad. Sci. USA* **106**, 16871–16876 (2009).
  59. Takeuchi, S., Kudo, T. & Takahashi, S. Molecular cloning of the chicken melanocortin 2 (ACTH)-receptor gene. *Biochim Biophys. Acta Mol. Cell Res.* **1403**, 102–108 (1998).
  60. Li, Y. et al. Molecular layer perforant path-associated cells contribute to feed-forward inhibition in the adult dentate gyrus. *Proc. Natl Acad. Sci. USA* **110**, 9106–9111 (2013).
  61. Tomer, R., Ye, L., Hsueh, B. & Deisseroth, K. Advanced CLARITY for rapid and high-resolution imaging of intact tissues. *Nat. Protoc.* **9**, 1682–1697 (2014). 2014 9:7.
  62. Chung, K. & Deisseroth, K. CLARITY for mapping the nervous system. *Nat. Methods* **10**, 508–513 (2013).
  63. Yang, B. et al. Single-cell phenotyping within transparent intact tissue through whole-body clearing. *Cell* **158**, 945–958 (2014).
  64. Kollmorgen, S., Hahnloser, R. H. R. & Mante, V. Nearest neighbours reveal fast and slow components of motor learning. *Nature* **577**, 526–530 (2020).
  65. de Marco Garcia, N. V. & Fishell, G. Subtype-selective electroporation of cortical interneurons. *J. Visualized Exp.* **42**, e51518 (2014).
  66. Wickersham, I. R., Finke, S., Conzelmann, K. K., & Callaway, E. M. Retrograde neuronal tracing with a deletion-mutant rabies virus. *Nat. Methods* **4**, 47–49 (2007).
  67. Klebes J. LoG Blob Detection. *GitHub* <https://github.com/jklebes/blob-detector/releases/tag/v1.1.0> (2024).
  68. Ferreira, T. A. et al. Neuronal morphometry directly from bitmap images. *Nat. Methods* **11**, 982–984 (2014).
  69. Arshadi, C., Günther, U., Eddison, M., Harrington, K. I. S. & Ferreira, T. A. SNT: a unifying toolbox for quantification of neuronal anatomy. *Nat. Methods* **18**, 374–377 (2021).
  70. Longair, M. H., Baker, D. A. & Armstrong, J. D. Simple Neurite Tracer: open source software for reconstruction, visualization and analysis of neuronal processes. *Bioinformatics* **27**, 2453–2454 (2011).
  71. Krupa, D. J., Matell, M. S., Brisben, A. J., Oliveira, L. M. & Nicolelis, M. A. Behavioral properties of the trigeminal somatosensory system in rats performing whisker-dependent tactile discriminations. *J. Neurosci.* **21**, 5752–5763 (2001).
  72. Yang, J. W. et al. Optogenetic modulation of a minor fraction of parvalbumin-positive interneurons specifically affects spatio-temporal dynamics of spontaneous and sensory-evoked activity in mouse somatosensory cortex in vivo. *Cereb Cortex* **27**, 5784–5803 (2017).
  73. Reyes-Puerta, V., Sun, J. J., Kim, S., Kilb, W. & Luhmann, H. J. Laminar and columnar structure of sensory-evoked multineuronal spike sequences in adult rat barrel cortex in vivo. *Cereb. Cortex* **25**, 2001–2021 (2015).
  74. Van Der Bourg, A. et al. Layer-specific refinement of sensory coding in developing mouse barrel cortex. *Cereb. Cortex* **27**, 4835–4850 (2017).

## Acknowledgements

We thank Yulia Gritsenko for genotyping, cryosectioning and for assisting along with Nadja Straumann in the anatomical tracings and Sholl analysis, Anna Cavaccini and Teyve Stachniak for their contribution in shaping the methodological approach in vitro, Jenq-Wei Yang for his contribution in setting up the equipment for the silicon probe recordings, Alina Mariuca Marinescu for assisting with the ISH and Martin Wieckhorst for their technical assistance. Slidescanner, confocal imaging and data analysis were performed with equipment maintained by the Center for Microscopy and Image Analysis (ZMB), University of Zürich. This work was supported by grants from the European Research Council (ERC, 679175, T.K.) the Swiss National Science Foundation (SNSF, 31003A\_170037 for T.K. and PZ00P3\_216312 for S.H.), the University Research Priority Program (URPP) Adaptive Brain Circuits in Development and Learning (AdaBD) of University of Zurich and the Swiss Government Excellence Scholarships (2018.0022, A.D.).

## Author contributions

A.D. performed electrophysiological experiments in vitro and in vivo, cryosectioning, stainings, injections, perfusions, wide field imaging, confocal and slide scanner imaging, electroporations, behavioral experiments, light-sheet imaging, data and statistical analysis, prepared figures and wrote the manuscript; L.C. collected most of the silicon probe and wide field data and assisted with the processing of the data; A.Ö.A. analyzed the in vivo wide-field imaging data and silicon probe recordings as well as created the computer vision and machine learning pipelines to analyze confocal and slide scanner imaging data; S.H. performed the analysis of the behavioral data; G.K. assisted with revisions, imaging and performed the NDNF and GAD1 ISH; M.K. assisted with revisions and analyzed the data collected from lightsheet imaging; O.H. injected RV to some Control mice at the young groups; L.G. assisted with the electroporations; S.K. developed the Dataspace software; F.H. provided access to equipment and input on the behavioral experiments and T.K. conceptualized the study, provided funding and wrote the manuscript.

## Competing interests

The authors declare no competing interests.

## Additional information

**Supplementary information** The online version contains supplementary material available at <https://doi.org/10.1038/s41467-024-50658-6>.

**Correspondence** and requests for materials should be addressed to Theofanis Karayannis.

**Peer review information** *Nature Communications* thanks the anonymous, reviewer(s) for their contribution to the peer review of this work. A peer review file is available.

**Reprints and permissions information** is available at <http://www.nature.com/reprints>

**Publisher’s note** Springer Nature remains neutral with regard to jurisdictional claims in published maps and institutional affiliations.



**Open Access** This article is licensed under a Creative Commons Attribution-NonCommercial-NoDerivatives 4.0 International License, which permits any non-commercial use, sharing, distribution and reproduction in any medium or format, as long as you give appropriate credit to the original author(s) and the source, provide a link to the Creative Commons licence, and indicate if you modified the licensed material. You do not have permission under this licence to share adapted material derived from this article or parts of it. The images or other third party material in this article are included in the article's Creative Commons licence, unless indicated otherwise in a credit line to the material. If material is not included in the article's Creative Commons licence and your intended use is not permitted by statutory regulation or exceeds the permitted use, you will need to obtain permission directly from the copyright holder. To view a copy of this licence, visit <http://creativecommons.org/licenses/by-nc-nd/4.0/>.

© The Author(s) 2024